What do dust sinks tell us about their sources and past environmental dynamics? A case study for oxygen isotope stages 3–2 in the Middle Rhine Valley, Germany

Mathias Vinnepand[1], Peter Fischer[1], Ulrich Hambach[2,3], Olaf Jöris[4], Carol-Ann Craig[5], Christian Zeeden[6], Barry Thornton[5], Thomas Tütken[7], Charlotte Prud'homme[8], Philipp Schulte[9], Olivier Moine[10], Kathryn E. Fitzsimmons[11], Christian Laag[12,13], Frank Lehmkuhl[9], Wolfgang Schirmer[14], and Andreas Vött[1]

[1]Natural Hazard Research and Geoarchaeology, Institute for Geography,
Johannes Gutenberg-Universität Mainz, 55099 Mainz, Germany
[2]BayCEER and Chair of Geomorphology, University of Bayreuth, 95440 Bayreuth, Germany
[3]Emil Racovita Institute of Speleology (ERIS), Romanian Academy, Cluj-Napoca branch,
Clinicilor 5, 400006 Cluj-Napoca, Romania
[4]MONREPOS Archaeological Research Centre and Museum for Human Behavioural Evolution,
Leibniz-Zentrum für Archäologie, 56567 Neuwied, Germany
[5]Environmental and Biogeochemical Sciences Group, The James Hutton Institute, Aberdeen, AB15 8QH, Scotland, UK
[6]Rock Physics and Borehole Geophysics, LIAG – Leibniz Institute for Applied Geophysics, 30655 Hanover, Germany
[7]Applied and Analytical Paleontology, Institute of Geosciences, Johannes
Gutenberg-Universität Mainz, 55099 Mainz, Germany
[8]Institute of Earth Surface Dynamics, University of Lausanne, 1015 Lausanne, Switzerland
[9]Chair in Physical Geography and Geoecology, Department of Geography, RWTH Aachen, 52056 Aachen, Germany
[10]Laboratoire de Géographie Physique, UMR 8591 CNRS Université Paris 1 UPEC, Thiais 94320, France
[11]Department of Geosciences, University of Tübingen, 72076 Tübingen, Germany
[12]Department of Research and Development, Nolte Geoservices GmbH, 48301 Nottuln, Germany
[13]Institut de Physique du Globe de Paris, CNRS, Université Paris Cité, 75238 Paris, France
[14]independent researcher: Wolkenstein 24, 91320 Wolkenstein, Germany

Correspondence: Mathias Vinnepand (mavinnep@uni-mainz.de) and Peter Fischer (p.fischer@geo.uni-mainz.de)

Abstract: The study of geological archives of dust is of great relevance as they are directly linked to past atmospheric circulation and bear the potential to reconstruct dust provenance and flux relative to climate changes. Among the dust sinks, loess–palaeosol sequences (LPSs) represent the only continental and non-aquatic archives that are predominantly built up by dust deposits close to source areas, providing detailed information on Quaternary climatic and terrestrial environmental changes. Upper Pleistocene LPSs of western central Europe have been investigated in great detail showing their linkage to

millennial-scale northern hemispheric climate oscillations, but comprehensive data on dust composition and potential source–sink relationships as well as inferred past atmospheric circulation patterns for this region are still fragmentary.

Here, we present an integrative approach that systematically combines sedimentological, rock magnetic, and bulk geochemical data, as well as information on Sr and Nd isotope composition, enabling a synthetic interpretation of LPS formation. We focus on the Schwalbenberg RP1 profile in the Middle Rhine Valley in Germany and integrate our data into a robust age model that has recently been established based on high-resolution radiocarbon dating of earthworm calcite granules. We show that Schwalbenberg RP1 is subdivided into a lower section corresponding to late oxygen isotope stage 3 (OIS; $\sim$ 40–30 ka) and an upper section dating into the Last Glacial Maximum (LGM; $\sim$ 24–22 ka), separated by a major stratigraphic unconformity. Sedimentological proxies of wind dynamics (U ratio) and pedogenesis (finest clay) of the lower section attest to comparable and largely synchronous patterns of northern hemispheric climatic changes supporting the overall synchronicity of climatic changes in and around the North Atlantic region. The anisotropy of magnetic susceptibility (AMS) reveals a clear correlation between finer grain size and increasing AMS foliation within interstadials, possibly owing to continuous accumulation of dust during pedogenic phases. Such a clear negative correlation has so far not been described for any LPS on stadial–interstadial scales.

Distinct shifts in several proxy data supported by changes in isotope composition (^{87}Sr/^{86}Sr and εNd) within the lower section are interpreted as changes in provenance and decreasing weathering simultaneously with an overall cooling and aridification towards the end of OIS 3 (after $\sim$ 35 ka) and enhanced wind activity with significant input of coarse-grained material recycled from local sources related to increased landscape instability (after $\sim$ 31.5 ka). We find that environmental conditions within the upper section, most likely dominated by local to regional environmental signals, significantly differ from those in the lower section. In addition, AMS-based reconstructions of near-surface wind trends may indicate the influence of north-easterly winds beside the overall dominance of westerlies. The integrative approach contributes to a more comprehensive understanding of LPS formation including changes in dust composition and associated circulation patterns during Quaternary climate changes.

Kurzfassung: Die Untersuchung geologischer Staubarchive ist von großer Bedeutung, da diese unmittelbar mit der atmosphärischen Zirkulation verknüpft sind und somit das Potenzial besitzen, sowohl Änderungen in der Staub-Herkunft als auch im Staubfluss in Verbindung mit Klimaänderungen zu rekonstruieren. Löss-Paläosol-Sequenzen (LPS) stellen in diesem Zusammenhang die einzigen kontinentalen nicht-aquatischen Archive dar, die sich aus Staubablagerungen bilden, die in relativer Nähe ihrer Liefergebiete liegen. Sie liefern zudem detaillierte Informationen über klimatische und terrestrische Umweltveränderungen im Quartär, die sich in Proxy-Daten der Staubzusammensetzung und der syn- und postsedimentären Veränderung widerspiegeln. Zwar belegen detaillierte Untersuchungen von LPS im westlichen Mitteleuropa direkte Verknüpfungen mit den jungpleistozänen Klimaschwankungen der nördlichen Hemisphäre, jedoch sind umfassende Daten zur Staubzusammensetzung und zur Kopplung von Staubquellen und -senken sowie zu den abgeleiteten atmosphärischen Zirkulationsmustern in der Region immer noch lückenhaft.

Unter Anwendung eines integrativen Ansatzes, der systematisch sedimentologische, gesteinsmagnetische und geochemische Daten kombiniert und durch Daten zur Isotopenzusammensetzung ergänzt wird, ist eine synthetische Interpretation der Bildung von LPS, hier am Beispiel des Profils RP1 am Schwalbenberg im Mittelrheintal, möglich. Wir verbinden unsere Daten mit einem detaillierten und robusten Altersmodell, das kürzlich auf der Grundlage hochauflösender Radiokohlenstoffdatierungen an Regenwurmkalziten (sog. Earthworm Calcite Granules, ECG) publiziert wurde. Auf Basis dieses Altersmodells kann gezeigt werden, dass das Profil RP1 in zwei Abschnitte, die durch eine deutliche Diskordanz getrennt sind, gegliedert wird. Der liegende Abschnitt entspricht dabei dem späten Sauerstoff-Isotopenstadium (OIS) 3 ($\sim$ 40–30 ka), während der hangende Abschnitt in das Letztglaziale Maximum (LGM) datiert ($\sim$ 24–22 ka). Für den liegenden Abschnitt zeigen die sedimentologischen Proxy-Daten (U Ratio, feinster Ton) vergleichbare und weitgehend synchrone Muster zwischen dem Schwalbenberg und Daten aus grönländischen Eisbohrkernen (NGRIP) und unterstützten somit die Annahme einer Synchronität von Klimaänderungen in und um den Nordatlantik.

Die Anisotropie der Magnetischen Suszeptibilität (AMS) zeigt in Interstadialen eine klare Korrelation kleinerer Korngrößen mit zunehmender AMS-Foliation, die möglicherweise auf kontinuierliche Staubakkumulation während der Pedogenese zurückzuführen ist. Ein solch klarer Zusammenhang wurde für LPS mit stadial–interstadialer Auflösung bisher nicht beschrieben.

Im liegenden Abschnitt von Profil RP1 am Schwalbenberg wird eine Abkühlung und Aridifizierung im späten OIS 3 (nach ∼ 35 ka) durch signifikante Änderungen in verschiedenen Proxy-Daten und der Isotopenzusammensetzung (^{87}Sr/^{86}Sr und εNd) deutlich, die auf unterschiedliche Staubquellen und abnehmende Verwitterung hindeuten. Zusätzlich führt eine erhöhte Instabilität der Landschaft in Richtung des LGM (nach ∼ 31,5 ka) zu verstärkter Windaktivität und dem Eintrag grobkörnigen Materials, das aus lokalen Quellen recycelt wurde.

Die Proxy-Daten des hangenden Abschnitts deuten auf Umweltbedingungen hin, die sich signifikant von jenen des Liegenden unterscheiden und vermutlich durch lokale bis regionale Einflüsse dominiert werden. AMS-basierte Rekonstruktionen der oberflächennahen Windtrends lassen neben der Dominanz von Westwinden auf einen phasenweisen Einfluss von Winden aus nordöstlicher Richtung schließen. Insgesamt sehen wir den vorgestellten integrativen Ansatz als einen wichtigen Beitrag zum besseren Verständnis der Bildung von LPS, welche die Veränderungen der Staubzusammensetzung und damit verbundener Zirkulationsmuster im Zuge quartärer Klimaänderungen besser beleuchtet.

1 Introduction

The production of mineral dust, its aeolian transport, and its deposition are important processes of the Earth–atmosphere system affecting the global radiative balance, changing the hydroclimate, and providing nutrients to both terrestrial and marine ecosystems (Muhs, 2013; Knippertz and Stuut, 2014; Marx et al., 2018). In order to understand potential links between dust flux and climate changes during the Quaternary, the study of geological archives of dust is of great relevance, as these are directly linked to past atmospheric circulation (Schaffernicht et al., 2020). As such they bear the potential to reconstruct dust provenance and dust flux relative to Quaternary climate changes whose proxies are frequently recorded in some of these archives (e.g. Mahowald et al., 2006; Újvári et al., 2016).

While ice, marine, and lake records are prominent Quaternary palaeoenvironmental and palaeoclimatic archives also tracing variations in atmospheric dustiness (e.g. Rasmussen et al., 2014; Sirocko et al., 2016; Kämpf et al., 2022), loess–palaeosol sequences (LPSs) represent the only continental and non-aquatic archive that is predominantly built up by dust deposits close to source areas (Muhs, 2013). They are thus providing detailed information on terrestrial palaeoenvironmental and palaeoclimatic change including dust composition and post-sedimentary alteration (e.g. Újvári et al., 2012; Schaetzl et al., 2018).

In western and central Europe, enhanced dust deposition during Upper Pleistocene stadial periods has been largely ascribed to increased fine particle production through glacial grinding activity, frost shattering, and entrainment of silty material from alluvial plains; glacial outwash plains; en-

dorheic basins; and exposed continental shelves (Frechen et al., 2003; Antoine et al., 2009; Smalley et al., 2009; Lehmkuhl et al., 2021; Pötter et al., 2021). In combination with gustier winds related to steepened meridional temperature gradients during stadial periods (McGee et al., 2010), the increased dustiness is reflected in peak dust accumulation especially during oxygen isotope stage (OIS) 2 along the western European loess belt (e.g. Frechen et al., 2003; Újvári et al., 2017; Fischer et al., 2021; Schmidt et al., 2021). This pattern is also observed in regional aquatic archives, such as maar lakes (e.g. Seelos et al., 2009; Fuhrmann et al., 2021) and supra-regional archives, such as Greenland ice cores (e.g. Rasmussen et al., 2014; Újvári et al., 2022).

In recent times, Upper Pleistocene key LPSs in western Europe have been investigated in great detail showing their linkage to northern hemispheric glacial–interglacial and millennial-timescale climate oscillations (e.g. Rousseau et al., 2007; Moine et al., 2017; Fischer et al., 2021; Prud'homme et al., 2022), but comprehensive data on dust composition and potential source–sink relationships as well as inferred palaeo-wind directions for this region are still scarce (e.g. Taylor et al., 2014; Schatz et al., 2015).

With this study we aim to contribute to a better understanding of dust provenance and past environmental dynamics using different methodological tools to investigate dust composition and to discuss potential source–sink relationships during late OIS 3 (∼ 40–30 ka) and parts of OIS 2 (∼ 24–22 ka) in western central Europe. Over the last few years, we were able to show that the Schwalbenberg LPSs in the Middle Rhine Valley in Germany resolve the last glacial cycle in exceptional temporal detail (Fischer et al., 2021; Vinnepand et al., 2022), proving previous studies that suggested

a linkage with the last glacial millennial-scale climate oscillations recorded in Greenland ice cores (Schirmer, 2000, 2011). Here, we focus on the 5.6 m deep section RP1, exposed at the southern edge of the Schwalbenberg. The RP1 profile was studied in detail by Fischer et al. (2021). Beside quantitative climate reconstructions based on the study of oxygen and carbon isotopes of earthworm calcite granules (ECGs), Bayesian age modelling based on radiocarbon dating of ECGs was used to establish a robust and reliable age model of the Schwalbenberg RP1 LPS (Prud'homme et al., 2022). Here, we use high-resolution sedimentological, rock magnetic, and bulk geochemical data to characterize dust composition along the stratigraphy. In addition, isotope geochemical measurements ($^{143}Nd/^{144}Nd$ and $^{87}Sr/^{86}Sr$) were conducted at lower resolution.

The U ratio, defined as the ratio of coarse versus medium plus fine silt, is employed to reconstruct wind dynamics and potential processes of sediment reworking (Vandenberghe et al., 1985; Vandenberghe, 2013). In addition, the finest clay content mostly reflects pedogenically formed clay (Schulte and Lehmkuhl, 2018) but potentially also dust components that have travelled longer distances (e.g. Muhs, 2013).

Beside such sedimentological data, the magnetic susceptibility evolved to an essential stratigraphic tool in the investigation of LPSs. As shown for many sites in Eurasia, magnetic susceptibility increases in palaeosols (magnetic enhancement), while relatively unaltered loess shows lower values. In contrast, lower magnetic susceptibility in palaeosols compared to loess is explained by the wind-vigour model (e.g. Evans and Heller, 2001); by waterlogging causing dissolution of iron minerals, which is mainly observed in loess affected by periglacial conditions (e.g. Taylor et al., 2014; Fischer et al., 2019); or by high amounts of primary magnetically enhanced sediments and their weathering products (von Suchodoletz et al., 2009; Obreht et al., 2016). In addition to low field bulk magnetic susceptibility (hereafter MS) the frequency-dependent magnetic susceptibility (hereafter MS_{fd}) is a qualitative parameter that allows us to determine the relative amount of newly formed ultrafine magnetic particles in the course of (incipient) pedogenesis (e.g. Buggle et al., 2014; Bradák et al., 2021). In the context of the reconstruction of past circulation patterns, the anisotropy of magnetic susceptibility (AMS) can additionally be utilized, which potentially reflects near-surface wind directions, if the primary magnetic fabric is preserved (Hrouda, 2007; Zhang et al., 2010; Taylor and Lagroix, 2015; Zeeden and Hambach, 2021).

In addition to these physical parameters, the bulk element composition is frequently employed to identify potential provenance shifts and sediment recycling as well as weathering intensity (cf. Buggle et al., 2011; Klasen et al., 2015; Profe et al., 2016; Vinnepand et al., 2022). In combination with Sr and Nd isotope geochemistry, which is a common tool in provenance studies (Grousset and Biscaye, 1989, 2005), potential changes in dust sources as well as secondary alteration of isotope signals may be detected in LPSs. While $^{143}Nd/^{144}Nd$ is a well-established provenance proxy that is strongly resistant to surface processes (e.g. weathering) (Goldstein and Jacobsen, 1988; Meyer et al., 2009; Grousset and Biscaye, 2005), $^{87}Sr/^{86}Sr$ might be prone to grain size effects (Feng et al., 2009) and to alteration through weathering (e.g. Clauer and Chaudhuri, 1995), potentially limiting a straightforward interpretation in terms of changing dust sources.

The systematic combination of these physical and geochemical proxy data opens the perspective for a comprehensive interpretation of LPS formation in the Middle Rhine Valley in Germany. Employing such an integrative approach, we aim to detect significant shifts in dust composition and discuss potential causes against the background of palaeoenvironmental and palaeoclimatic oscillations during the time period investigated.

2 Regional setting and stratigraphy

The Schwalbenberg site in the Middle Rhine Valley is located in the centre of the Rhenish Massif (Germany; 50.562378° N, 7.240425° E; −90–135 m a.s.l. – above sea level; Fig. 1). Up to 30 m thick Upper Pleistocene LPSs drape the lower middle terrace 1 (LMT 1) of the penultimate glaciation (cf. Boenigk and Frechen, 2006) and at least two further, older terrace levels of the Rhine, overall resolving Atlantic-driven Upper Pleistocene climate oscillations in more detail than any other terrestrial archive in the region described so far (Fischer et al., 2021). Nowadays, the area is characterized rather by a maritime climate influence (mean annual temperature: 10.2 °C; mean annual precipitation: 643 mm; Deutscher Wetterdienst, 2023), with low-air-pressure systems predominantly entering the area from the Atlantic to the west (Prud'homme et al., 2022).

During the Upper Pleistocene the site was situated between the glaciated Alps in the south; the Fennoscandian (FIS) and British–Irish ice sheets (BIIS) in the north, which reached their maximum extents during the Last Glacial Maximum (LGM) (e.g. Lambeck et al., 2014); and the – at this time – dried out plains of the English Channel westward and north-westward (Fig. 1), all of which are considered important dust-producing and dust source areas for LPSs in western and central European periglacial realms (Antoine et al., 2009; Lehmkuhl et al., 2021; Baykal et al., 2022). In addition, the alluvial plains of – over long periods – braided river systems, here the Rhine and its tributaries, are assumed to represent major regional dust sources during stadial phases (e.g. Schatz et al., 2015; Rousseau et al., 2018).

Furthermore, the Rhenish Massif itself experienced intensive frost-weathering in the most severe cold periods of the Pleistocene and intensive sediment relocation under cold and humid conditions, forming Pleistocene periglacial slope deposits (PPSDs) (Sauer and Felix-Henningsen, 2006), rep-
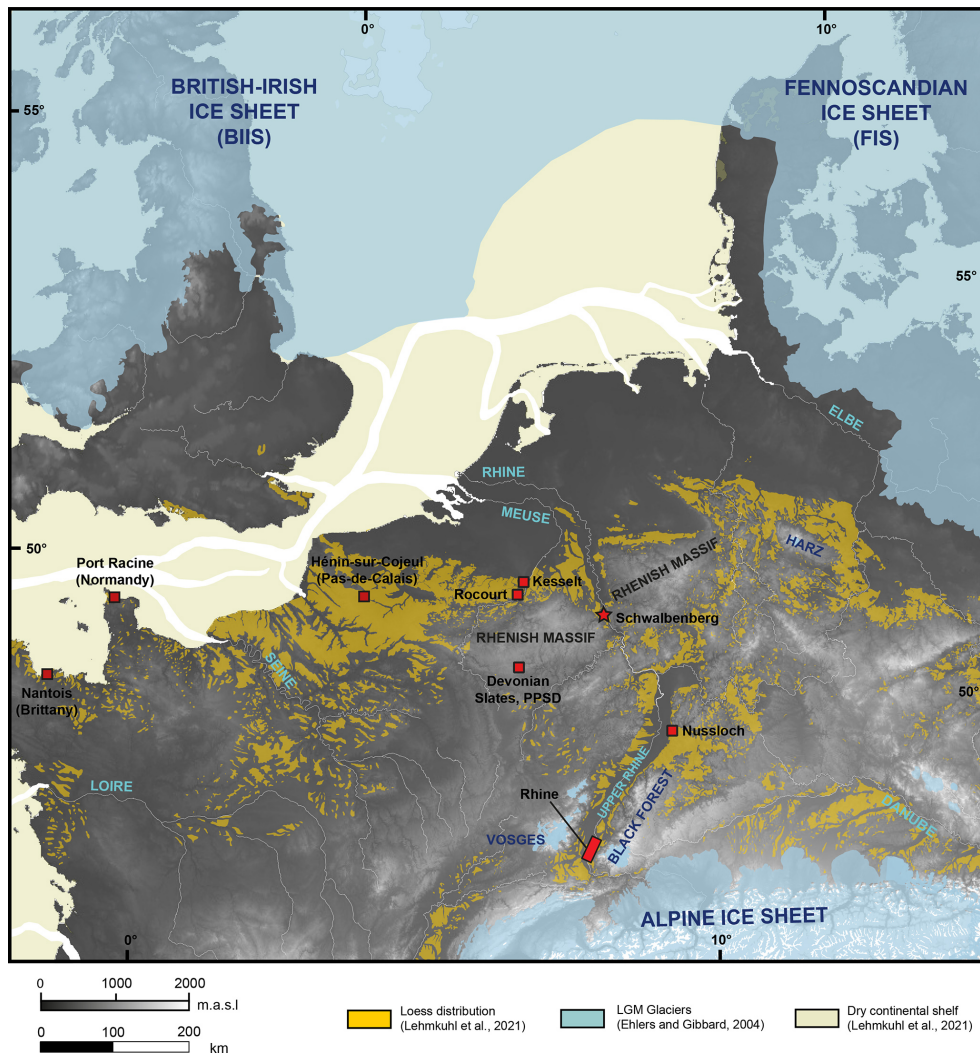
Figure 1. Map based on the digital elevation model (GLOBE 1.0) showing western central Europe during the Last Glacial Maximum (LGM, centred at ∼ 22 ka); the location of the Schwalbenberg site in the Middle Rhine Valley, Germany; and selected key sites (see text for explanation). The Schwalbenberg site is located between the Alpine ice sheet in the south and the Fennoscandian and British–Irish ice sheets in the north.

resenting potential subordinated local dust sources (Janus, 1988; Römer et al., 2016).

During the Upper Pleistocene, the Schwalbenberg site was located close to the alluvial plains of the braided systems of the rivers Ahr and Rhine, reflecting possible sources of mineral dust of local to regional origin. The comparably small Ahr River catchment ($6.63 \, \text{m}^3 \, \text{s}^{-1}$ mean annual discharge; Ministry for Environment RLP, 2021) is located in the northern parts of the Eifel area where Devonian rocks (mostly schistose clayey silt- and sandstones and subordinated limestones) are predominant (Meschede, 2018; Fig. 2). In contrast, the Rhine catchment until the mouth of the Ahr ($2010 \, \text{m}^3 \, \text{s}^{-1}$ mean annual discharge ∼ 20 km south of Schwalbenberg; International commission for the hydrology of the Rhine basin, 2021) includes the north-western Alps

and the Upper Rhine Graben (with small tributaries draining parts of the Vosges, Black Forest, and Odenwald), as well as its main tributaries with the rivers Neckar (draining parts of the Swabian Alb, Triassic Keuperbergland (Keuper Uplands), Black Forest, and Odenwald), Main (draining the Fichtel Mountains, Franconian Alb, and several other Franconian uplands), Lahn (draining the Rhenish Massif), Nahe (draining predominantly the Saar–Nahe basin), and Mosel (draining parts of the Vosges, the easternmost Paris Basin, and the Rhenish Massif) (Meyer and Stets, 1996; Fig. 2).

In this study, we focus on the 5.60 m thick RP1 profile located at the southern fringe of the Schwalbenberg facing the Ahr valley (Figs. 3, 4). The profile was described and subdivided into 21 stratigraphic units (SUs), correlated to superordinate stratigraphic units (SSUs) D, E, and F within the gen-
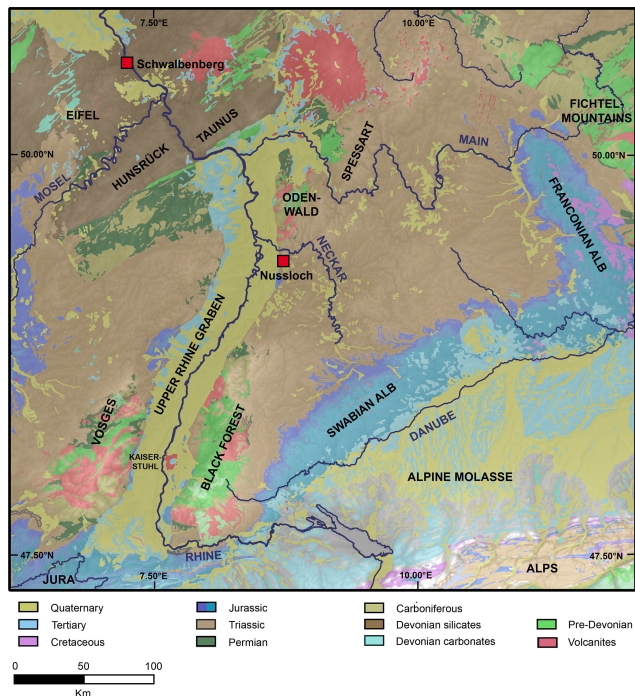
Figure 2. Geological map showing the main geological units of the Rhine catchment up to the Lower Rhine Embayment (Federal Institute for Geosciences and Natural Resources Germany, 2022). Calcareous rocks and sediments dominate the Rhine catchment in the northern Alps and the Molasse basin. The flanks of the Upper Rhine Graben include volcanites and metamorphic pre-Devonian rocks as well as Triassic siliciclastics and carbonates. The Rhenish Massif is dominated by Devonian slates and sandstones, and subordinated Devonian limestones occur.

Figure 3. (a) Map of the Lower Middle Rhine Valley in western central Germany based on the digital elevation model (DEM based on SRTM 30 data by USGS (2022). The Schwalbenberg site is located north-west of the confluence of the Rhine and the Ahr. These river systems are the most important source areas of mineral dust. **(b)** The inset map (BingMaps, 2021) shows the position of the REM 3 key LPSs and the RP1 section (cf. Fischer et al., 2021; Prud'homme et al., 2022).

correlated to OIS 2 between ∼ 24 000 and 21 900 cal BP (see Sect. 3.5).

3   Materials and methods

Continuous sampling in 2 cm intervals was performed for grain size, bulk geochemical, and rock magnetic analyses including the determination of the anisotropy of magnetic susceptibility (AMS). However, the latter was conducted for every second sample (see Sect. 3.3). In addition, we collected 30 samples with 5 cm sampling width for Sr and Nd isotope analyses according to stratigraphy (see Fig. 4 for sample distribution, sampling intervals are given in Table S2).

3.1   Laser granulometry

We analysed the grain size of samples from the Schwalbenberg RP1 profile to calculate the U ratio and finest clay proportion. The U ratio is defined as the ratio of coarse versus medium and fine silt (Vandenberghe et al., 1985; Újvári et al., 2016) and is used to discriminate between sediments that were transported by dynamic and relatively strong winds (high U ratio) and those transported by weaker winds (low U ratio) (Vandenberghe et al., 1997). The finest clay proportion (fCl < 0.2 μm) mainly reflects post-depositional

eral Schwalbenberg stratigraphic model (Fischer et al., 2021; see Table 1). The SSUs were defined by lithology and by the classification of palaeosols according to the IUSS Working Group WRB (Schad et al., 2015).

High-resolution radiocarbon dating on ECGs confirm that the lower section of the sequence covers late OIS 3, which is characterized by the formation of Calcaric Cambisols at Schwalbenberg correlated to Greenland Interstadials (GIs) 8–6 (cf. Fischer et al., 2021; Prud'homme et al., 2022). The Calcaric Cambisols of SUs 2–6 build a soil complex, whilst the uppermost Calcaric Cambisol (SU 8), correlated to GI 6, is clearly separated from the previous one by a loess layer (SU 7).

Based on the RP1 age model (Prud'homme et al., 2022), the Gelic Gleysol of SU 11 covers the transition from GI 5.2 to Greenland Stadial (GS) 5.2. A formation during milder climate conditions during GI 5.2 is likely. The next loess layer of SU 12 is truncated due to erosion prior to accumulation of the upper section represented by SSU F.

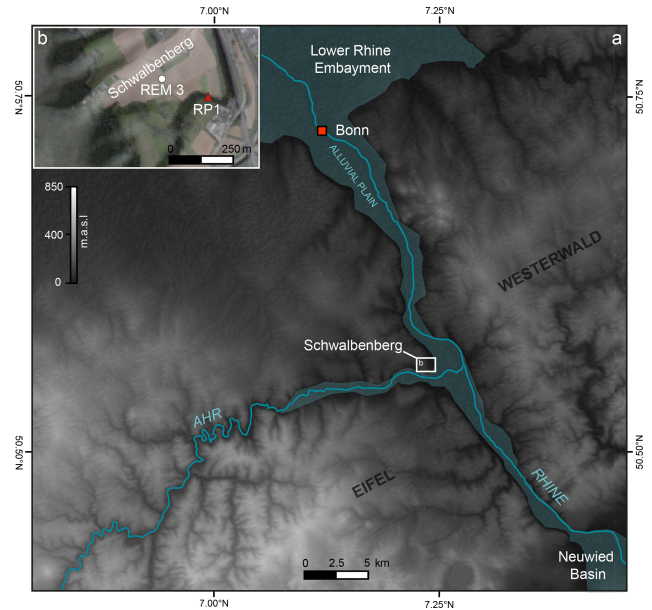SSU F above the unconformity (base of SU 13) contains reworked loess, loess, and weakly developed Gelic Gleysols
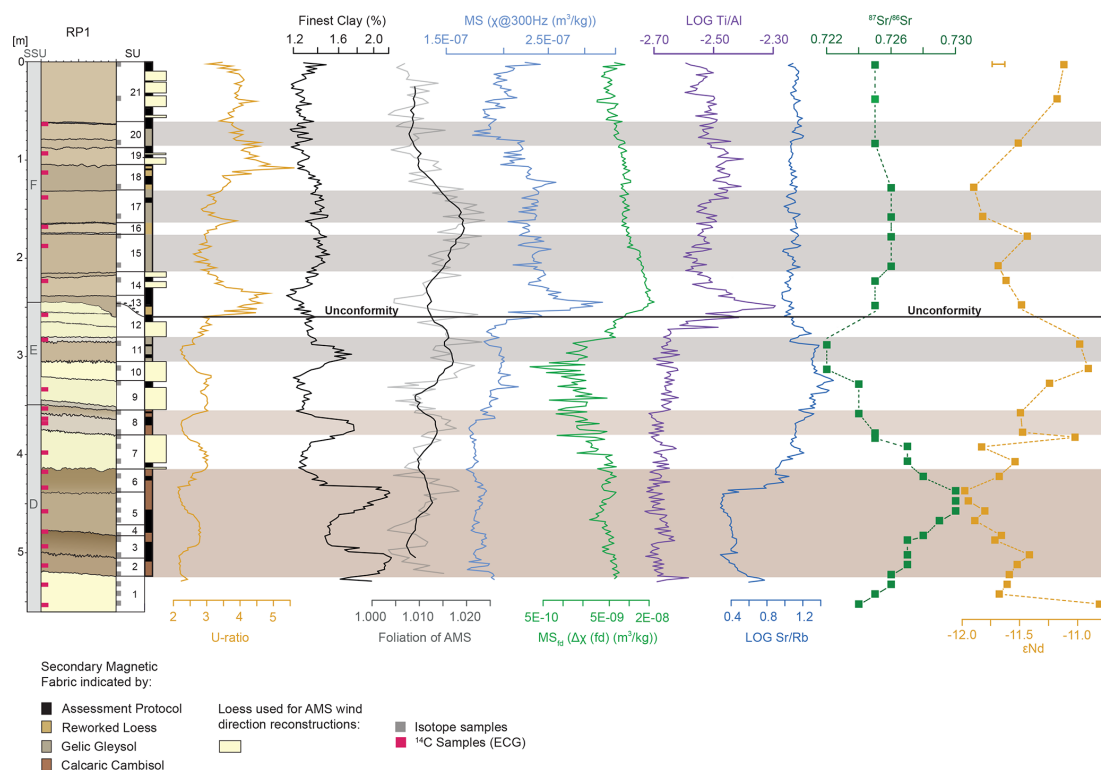
Figure 4. From left to right: stratigraphic log of profile RP1 and positions of ECG samples used for radiocarbon dating (modified after Prud'homme et al., 2022; radiocarbon ages are given in Table 1). SSUs and SUs are given according to Fischer et al. (2021); log depicting secondary magnetic fabric and loess layers used for AMS-based reconstruction of near-surface wind directions following the statistical assessment (see Supplement for details); grain size data: U ratio and finest clay; magnetic fabric and environmental magnetism: foliation of the AMS, MS (χ @300 Hz), and MS$_{fd}$ ($\Delta\chi$ (fd)); geochemical data: log Ti/Al and log Sr/Rb; isotope geochemistry: ^{87}Sr/^{86}Sr and εNd. Sr and Nd isotope sampling positions are indicated by grey squares next to the stratigraphic log of SUs, and 2σ for internal basalt standard measurements (reproducibility) is below the size of the sample symbols for ^{87}Sr/^{86}Sr but exceeds these for εNd (see scale in the data plot). For the calculation, statistics and uncertainty of AMS data, and details on sample reproducibility of isotope measurements, we refer the reader to the Supplement.

grain size reduction by chemical weathering (Schulte and Lehmkuhl, 2018).

We undertook granulometry using a laser diffraction particle size analyser (LS 13 320 PIDS, Beckman Coulter) to analyse non-decalcified samples (cf. Schulte et al., 2016). Sample pre-treatment involved removal of organic carbon by 0.70 mL 20 % H_2O_2 and dispersion with 25 mL of $Na_4P_2O_7$ at 0.1 mol L^{-1} for 12 h (Jones, 2003; Blott et al., 2004). Quadrupole measurements using two different concentrations ensured high precision. Through data processing, we applied the Mie theory (fluid RI: 1.33; sample RI: 1.55; imaginary RI: 0.1; Jones, 2003; Ozer et al., 2010).

3.2 Bulk geochemistry

We integrated the Ti/Al ratio as a provenance indicator, as both elements are relatively immobile and their ratio is not significantly affected by weathering or pedogenesis (e.g. Zech et al., 2008; Sheldon and Tabor, 2009). In addition, we complementarily use the Sr/Rb ratio as an indi-

cator of weathering intensity based on the assumption that Sr shows an analogous behaviour to Ca being easily soluble and mobile in the course of weathering, while Rb behaves relatively immobile under moderate weathering conditions due to strong adsorption to clay minerals (e.g. Buggle et al., 2011). We are aware of the fact that the initial Sr/Rb ratio is maybe partly masked by the dynamics of carbonate-bound Sr in the course of secondary carbonate precipitation (e.g. Buggle et al., 2011; Profe et al., 2016), the latter effect being detailed by Vinnepand et al. (2020) for the Schwalbenberg LPS.

We determined element composition with a polarization energy dispersive X-ray fluorescence (EDP-XRF) spectrometer (Spectro Xepos, Spectro) onto pressed sample pellets (bulk sediments < 2 mm) (see Vinnepand et al., 2022). Measurements were performed in duplicates to ensure data quality (measurements were excluded in the case when duplicates exceeded 3σ). We used the decadic logarithm (log ratios) of element ratios for data symmetry and to overcome the closed sum constraint (Weltje et al., 2015; Profe et al., 2016). For

Table 1. Subdivision of the RP1 profile into superordinate stratigraphic units (SSUs) F, E, and D (lower (older) SSUs are not exposed at RP1) and stratigraphic units (SUs) and their corresponding lithological and pedological interpretation (see Fischer et al., 2021, for further details). The ages were published by Prud'homme et al. (2022) based on radiocarbon dating applied to 22 ECG samples, and the calibration was based on IntCal20 (Reimer et al., 2020). The Greenland events are shown according to the INTIMATE event stratigraphy (Rasmussen et al., 2014). The radiocarbon ages have been integrated into Bayesian age modelling (Prud'homme et al., 2022) using the Bacon software (Blaauw and Christeny, 2011). The age model is integrated into Fig. 6 in the Discussion section.

Profile RP1	SSU	SU	Lithology/pedology	Age (cal BP) min–max (2σ)	Greenland events
Upper section	F	21	Loess	–	
	F	20	Gelic Gleysol	21 426–22 150	GS 2.1a
	F	19	Loess	22 327–22 500	GS 2.1a
	F	18	Reworked loess	22 424–22 652	GS 2.1a
	F	17	Gelic Gleysol	22 557–22 846	GS 2.1a
	F	16	Reworked loess	22 793–23 073	GS 2.1a
	F	15	Gelic Gleysol	23 079–23 663	GI 2.2
	F	14	Loess	23 863–24 619	GS 3
Unconformity (base of SU 13)	F	13	Reworked loess	–	–
Lower section	E	12	Loess	30 199–30 970	GS 5.2/GI 5.1
	E	11	Gelic Gleysol	31 128–32 018	GI 5.2/GS 5.2
	E	10	Loess	–	GI 5.2/GS 5.2
	E	9	Loess (partly laminated)	31 862–33 931	GS 6/GI 5.2
	E	9	Loess (partly laminated)	32 562–33 412	GI 6/GS 6
	E	9	Loess (partly laminated)	32 922–33 614	GI 6/GS 6
	D	8	Calcaric Cambisol	33 077–33 703	GI 6
	D	7	Loess	33 728–34 310	GS 7
		6		34 749–34 153	GI 7/GS 7
	D	6		35 134–34 453	GI 7/GS 7
	D	5	Soil complex (Calcaric	34 879–35 675	GI 7
	D	4	Cambisols, SU 2–6)	35 298–36 380	GS 8
	D	3		36 406–37 473	GI 8
	D	2		36 826–38 129	GI 8
	D	1	Loess	37 374–38 873	GS 9
	D	1	Loess	38 162–39 963	GS 9

integrating the element concentrations of Sr and Nd in the context of mixing equations (cf. Faure and Mensing, 2005), we applied XRF measurements to the same samples used for isotopic measurements (see Sect. 3.4).

3.3 Magnetic susceptibility and anisotropy of magnetic susceptibility

Since the 1980s environmental magnetic parameters have been recognized as fundamental palaeoclimate proxies for Eurasian LPSs, and low field magnetic susceptibility (MS) was established as a stratigraphic tool, facilitating correlations between terrestrial deposits and the marine record. The latter is based on stratigraphic oxygen isotope data for oceanic foraminifera, which in turn is a proxy for global ice volume (e.g. Evans and Heller, 2003; Liu et al., 2012). The frequency dependency of magnetic susceptibility (MS_{fd}), also expressed as the absolute difference of χ @ 300 Hz and χ @ 3000 (Hz χ @ 300 Hz–χ @ 3000 Hz $= \Delta\chi$), provides in-

formation on magnetic grain size spectra and may allow for the assignment of magnetic enhancement to soil formation processes to wind vigour effects and depletion due to hydromorphy in comparison to the low field MS (Forster et al., 1994; Bradák et al., 2021).

Furthermore, MS in LPS deposits has one additional application. Directional measurements of MS on oriented samples are used for fabric analyses. The AMS (anisotropy of magnetic susceptibility) method is an established structural indicator even in unconsolidated geological materials (Bradák et al., 2020). Magnetic fabric can be correctly approximated by a second-order symmetric tensor and fabric magnitude (i.e. degree of anisotropy) and fabric shape (i.e. prolate or oblate). Additionally, the orientation of principal axes of AMS ellipsoids (K_{MAX}, K_{INT}, K_{MIN}) can be used for fabric characterization and quantification (Hrouda, 2007).

In order to study the natural physical properties of the undisturbed sedimentological fabric, we collected oriented samples (cube edge lengths 2 cm, hence 8 cm^3 sample vol-

ume) exhibiting a ~ 2.1 cm vertical spacing of their centres (Zeeden et al., 2015; Zeeden and Hambach, 2021). The volume MS was measured using a susceptibility bridge (VFSM; Magnon, Germany) at AC fields of $300\,\mathrm{A\,m^{-1}}$ at 300 and 3000 Hz, respectively. Subsequently, the resulting values were mass normalized and given as mass-specific MS (χ) (cf. Buggle et al., 2014; Zeeden et al., 2018). Every second sample (~ 4.2 cm stratigraphic resolution) was subject to AMS measurements using a MFK1-FA kappabridge (AGICO) in a $400\,\mathrm{A\,m^{-1}}$ and 976 Hz alternating field and a rotator. We visualized the results of AMS measurements as a magnetic susceptibility ellipsoid with three orthogonal principal axes: the maximum axis (K_{MAX}), the intermediate axis (K_{INT}), and the minimal axis (K_{MIN}) by using the Anisoft v. 5.0.18 software supplied by AGICO. The magnetic susceptibility ellipsoid defines the overall magnetic fabric of a rock sample, reflecting the statistically preferred orientation of mineral grains. In this study, we employed the most common anisotropy parameters that are used to investigate the nature of magnetic fabrics in LPS, i.e. lineation (L) and foliation (F) describing the shaped and oblateness of an AMS ellipsoid, respectively. The data are presented in rose diagrams of K_{MAX} and stereoplots displaying the full spatial orientation of K_{MAX}, K_{INT}, and K_{MIN}. The applied assessment protocol (see Fig. 4) and associated statistical analyses are detailed in the Supplement.

3.4 Strontium and neodymium isotope geochemistry

The original Sr and Nd isotope compositions of igneous rocks represent fingerprints for their petrogenesis (e.g. preferential partitioning of incompatible Nd and Rb into the melt and compatible Sm and Sr into the solid residue during magmatic differentiation) and age (radioactive decay of ^{87}Rb to ^{87}Sr and ^{147}Sm to ^{143}Nd) (DePaolo and Wasserburg, 1976; Goldstein et al., 1984; Grousset and Biscaye, 1989). This leads to characteristic ^{143}Nd/^{144}Nd (εNd) and ^{87}Sr/^{86}Sr isotope signatures in crustal and mantle rocks, with felsic rocks having high ^{87}Sr/^{86}Sr and low ^{143}Nd/^{144}Nd (εNd) and the inverse for mafic (mantle-derived) rocks (εNd represents the original measured ^{143}Nd/^{144}Nd normalized to the chondritic uniform reservoir 0.512638 (CHUR, $t = 0$) (Faure and Mensing, 2005) following the equation

$$\varepsilon\mathrm{Nd} = (^{144/143}\mathrm{Nd}\,\mathrm{sample}/^{144/143}\mathrm{Nd}\,\mathrm{CHUR} - 1) \times 10\,000. \quad (1)$$

Older rocks of similar mineralogical composition have more radiogenic ^{87}Sr/^{86}Sr and εNd due to prolonged radioactive decay. Sediments forming through physical weathering of crustal rocks inherit the isotope composition of their bedrock (Goldstein and Jacobsen, 1988, 1987). The Sr isotope composition in a dust sink may differ from the source due to mineral sorting e.g. during (aeolian) transport (Újvári et al., 2012), and selective depletion of Sr-bearing minerals during chemical weathering (e.g. Drouet et al., 2007). Hence, more soluble Sr-rich minerals such as carbonates may change the

original ^{87}Sr/^{86}Sr bulk sediment composition. In contrast, εNd is strongly resistant to surface weathering and grain size sorting effects (Meyer et al., 2009; Újvári et al., 2012; Wang et al., 2007; Zhu et al., 2021), still reflecting the original or rather unchanged source rock composition. Prior to sample digestion, we dissolved pedogenic calcites while preserving clay minerals (0.5 M acetic acid) (Újvári et al., 2012). For sample digestion, we used 6 mL of 48 % HF (AR grade) and 1 mL of trace grade 68 % HNO$_3$ and heated the mixture at 150 °C in Teflon bombs. Purified Sr and Nd fractions were used to determine ^{143}Nd/^{144}Nd and ^{87}Sr/^{86}Sr using an Isotopix Phoenix TIMS (thermal ionization mass spectrometer) device through multi-dynamic analyses. For quality control, we ran the NIST SRM 987 reference material (^{87}Sr/^{86}Sr = 0.710255 ± 0.000013 at 2σ, $n = 5$) for Sr and the JNdi-1 reference material (^{143}Nd/^{144}Nd = 0.512103 ± 0.000004 at 2σ, $n = 7$) for Nd. The average standard error for 100 ratios of data for each of the samples is 0.000011 for ^{87}Sr/^{86}Sr and 0.000002 ± 2 SE for ^{143}Nd/^{144}Nd (for more information on sample preparation, purification, and quality control, please see Supplement).

3.5 Age modelling

Prud'homme et al. (2022) constrained the time span of a distinct unconformity at the base of SU 13 as a ~ 5–6 kyr hiatus spanning 30 970–30 199 to 24 619–23 863 cal BP, based on the closest radiocarbon ages below and above the unconformity, respectively (see Table 1). Quantitative climate reconstructions and the age model presented in Prud'homme et al. (2022) were related to the stratigraphical positions of the ECG samples chosen for either stable isotope analyses or radiocarbon dating, whereof no samples were taken from SU 13 and the lower part of SU 14 (both SUs located above the unconformity). Here, we performed continuous sampling in 2 cm intervals for grain size, bulk geochemical, and rock magnetic analyses. Thus, we produced a continuous analytical data set along a discontinuous age model. To account for this, we also integrated the stratigraphic information as described by Fischer et al. (2021). Based on their litho- and pedostratigraphic model, the erosional phase causing the hiatus in section RP1 must have taken place with or shortly after the deposition of the Eltville tephra. This tephra, whose average age is around 24.3 ka (Zens et al., 2017; Förster et al., 2020), is an important stratigraphic marker found in many western European LPSs (e.g. Meijs et al., 1983). We then re-calculated the age model with 2 cm intervals using the Bacon software (Blaauw and Christeny, 2011) and the IntCal20 calibration curve (Reimer et al., 2020). For the profile section from 260 cm (base of SU 13 = unconformity) to 222 cm below surface (position of the first radiocarbon sample above the unconformity), we assume a continuous age decrease with depth, ranging from 24 300 to 23 945 cal BP.

With regard to our interpretation of the proxy data plotted against the age model (Fig. 6), we are aware that age uncer-
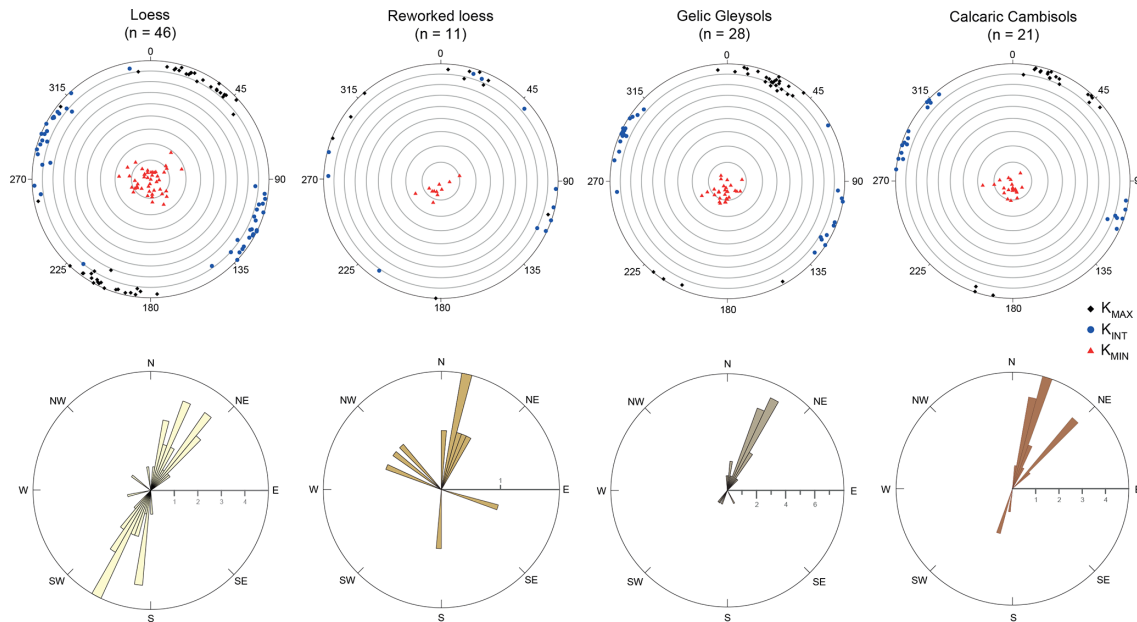
Figure 5. Stereoplots showing the full spatial orientation of K_{MAX}, K_{INT}, and K_{MIN} and rose diagrams of the lineations for all samples that passed the criteria as outlined (Fig. 4 and Sect. S1 in the Supplement) and the subsets for loess, reworked loess, Gelic Gleysols, and Calcaric Cambisols. See Figs. S1 and S2 for a comparison of all samples for each sediment type.

tainties occur both in the radiocarbon-based age model and in the INTIMATE (INTegration of Ice-core, MArine and TErrestrial records) event stratigraphy. In the latter, for instance, the maximal counting error for GI 5.2 is 1024 years (Rasmussen et al., 2014) and thus in a similar range as the errors in the underlying Bacon age model.

4 Results

4.1 Down-profile variation in selected proxy data

A clear subdivision of the RP1 profile is visible in all selected proxies. Based on significant sedimentological changes in the stratigraphical succession, a lower section (SUs 1–12) reaching to the unconformity and an upper section above the unconformity (SUs 13–21) are distinguished (Fig. 4). The U ratio shows maxima in the loess layers (SUs 7, 9, 10, 12) and in the middle of the basal soil complex (SUs 1–6), while the finest clay shows an inverse behaviour with distinct maxima in all well-developed palaeosols. Above the unconformity, the variations in clay content are significantly lower, showing a minimum at the transition from SU 13 to 14 and weak maxima in the Gelic Gleysols of SUs 15 and 17. In contrast, the U ratio shows higher and significant variations with absolute maxima in SUs 13 and 18 and weak minima in the Gelic Gleysols (SUs 15 and 17). Throughout the profile and especially below the unconformity, minima in the U ratio and maxima in the finest clay correspond to increased foliation values.

The MS shows low variations in the entire lower part, with a slight decrease from the base to the midst of SU 8, followed by slight increases towards the midst of SU 11 from where it slightly decreases again. Obviously, palaeosols and loess layers are not clearly differentiated. The MS_{fd} shows an overall decrease from the base to SU 11, with increased amplitudes above SU 6 and an inverse trend compared to the MS from the top of SU 8 to SU 11. In the top part of SU 11, the values significantly increase towards the unconformity. In SU 13 both MS and MS_{fd} reach maximum values, whereof the MS forms a distinct peak. Above, the MS shows minima in SUs 15, 17, and 20, where intensive hydromorphic staining has been observed. Another maximum is observed at the base of the reworked loess of SU 18, while the MS_{fd} is continuously decreasing towards the top of the sequence. Log Ti/Al shows minor variations throughout the lower section, with slightly increasing values on top of the Calcaric Cambisol of SU 8. As described for the MS and MS_{fd}, also log Ti/Al increases towards the unconformity and above, again forming a distinct maximum in SU 13. Generally lowered values are observed until the top of SU 17 and above SU 19, with higher values in between. Log Sr/Rb shows the lowest values in the well-developed palaeosols of the basal soil complex. From the top of SU 5 the values increase, before they newly decrease from the top of SU 11 towards the unconformity. Remarkably, the MS and log Sr/Rb show a high correlation from SU 7 to SU 11. Above the unconformity, log Sr/Rb shows no significant variations. Both the ^{87}Sr/^{86}Sr ratio and εNd cover a relative restricted range from 0.722 to 0.730 and from −10.77 to −11.98, respec-

tively. The ^{87}Sr/^{86}Sr ratio increases from the base until SU 6. In contrast, apart from the lowermost sample εNd follows this trend until SU 3 but turns into the opposite trend thereafter, reaching the absolute minimum at the base of SU 6, accompanied by the absolute maximum of ^{87}Sr/^{86}Sr. Towards the unconformity, both ^{87}Sr/^{86}Sr and εNd show an inverse behaviour with decreasing ^{87}Sr/^{86}Sr and increasing εNd values. Above the unconformity, throughout the upper section only minor variations in ^{87}Sr/^{86}Sr occur. In contrast, εNd overall decreases towards the base of SU 18, apart from one peak at the top of SU 16. From the base of SU 18 it increases again until the top of the sequence, thus being decoupled from ^{87}Sr/^{86}Sr in the upper part of the sequence.

To sum up, all proxy records indicate not only significantly differing characteristics below and above the unconformity but also a clear change starting in the upper part of the Gelic Gleysol of SU 11.

4.2   Magnetic fabric

Overall, the preferential direction of the lineation of all samples that passed the assessment protocol (see Fig. 4, Sect. S1) is SSW to NNE (Fig. 5). This is also true for datasets comprising all samples (Figs. S1, 2). All stereoplots show a horizontal plain defined by K_{MAX}, K_{INT}, and K_{MIN} plotting perpendicular to this plain and close to the vertical axis. It should be noted that the principal axes of the AMS ellipsoids and the resulting lineations are linears and not vectors, as they do not indicate a distinct direction but only an alignment. For example, an NE-pointing trend in the rose diagrams is equivalent to a SW trend and vice versa, as the diagram is to be read point-symmetrically. In the rose diagrams of lineation and stereoplots, the loess units indicate clear populations ($\sim$ 15 to $\sim$ 45° and $\sim$ 195 to $\sim$ 225°) aligned $\sim$ NE-SW. However, reworked loess exhibits a second subordinate direction perpendicular to the main direction ($\sim$ NNE–SSW), possibly reflecting multiple water-runoff and sediment reworking effects (cf. Tarling and Hrouda, 1993). The Gelic Gleysols show a clear dominance of NNE–SSW lineations, and the Calcaric Cambisols show a preferential trend of lineations scattering between NNE–NE and SSW–SW. Further information on the AMS results is given in the Supplement.

5   Discussion

5.1   Stratigraphic interpretation of proxy data

In order to comprehensively discuss our results, all Schwalbenberg RP1 proxy data were plotted against the radiocarbon-derived Bayesian age model (Fig. 6) accomplished by sedimentation rate and precipitation quantification (Prud'homme et al., 2022). Schwalbenberg RP1 is subdivided into a lower section that covers the period from the end of GS 9 until the end of GS 5.2 ($\sim$ 39 200–30 800 cal BP) and an upper section covering the last third of GS 3 until

GS 2.1 ($\sim$ 24 300–21 900 cal BP). In the lower section, well-developed palaeosols and loess layers particularly resolve the period from GIs 8–5.2 and corresponding GSs, respectively. Ranging between 2 and 3, the U ratio shows values typical for central European LPSs, with lower values during interstadials related to reduced wind activity and higher values during stadials indicating gustier winds (e.g. Vandenberghe, 2013; Kämpf et al., 2022).

The basal soil complex (SUs 2–6) contains well-developed Calcaric Cambisol horizons depicted by two distinct clay peaks and lowest Sr/Rb values, attesting intensive weathering and pedogenesis. In this context, the increase in ^{87}Sr/^{86}Sr is unlikely to predominantly reflect provenance changes due to its susceptibility to weathering impacts (cf. Clauer and Chauduri, 1995), while the distinct shift in εNd might be related to a dust source signal (see Sect. S4).

The first clay maximum is followed by an increase in the U ratio and a distinct peak in the sedimentation rate, corresponding to the second half of GI 8. After a short decline, the Schwalbenberg sedimentation rate increases in tandem with elevated dust probabilities in the nearby Eifel maar lakes (Eifel Laminated Sediment Archive, ELSA, dust probability; Seelos et al., 2009), indicating continuous dust input until the beginning of GI 5.2. This pattern diverges from the trend recorded in the North Greenland Ice Core Project (NGRIP), where high Ca^{2+} values relate to GSs and distinct minima to GIs. This difference supports the idea of an accretionary character of the Schwalbenberg LPSs in general and the palaeosols in particular, as described by Vinnepand et al. (2020) and Fischer et al. (2021).

After GI 7, clay contents in RP1 generally decrease but still peak within the palaeosols of GI 6 (Calcaric Cambisol) and GI 5.2 (Gelic Gleysol). The U ratio follows exactly the opposite trend, showing overall coarsening. Hence, this indicates enhanced wind activity from GS 7 onwards, with clear maxima during GSs and reduction during GIs, respectively.

The MS_{fd} shows overall decreasing values from SU 1 up to the base of SU 11, indicating a continuous reduction in fine magnetic particles. As MS is contemporaneously increasing (Fig. 4), we assume that this opposite trend is related to a domination of wind vigour over pedogenesis (e.g. Evans and Heller, 2001). This is also supported by high U ratio values especially in loess layers (SUs 9 and 10) and a strong increase in log Sr/Rb, indicating reduced weathering and input of primary carbonates at the same time (see Vinnepand et al., 2020; Fischer et al., 2021).

Log Ti/Al, which is interpreted to relate to provenance (Zech et al., 2008; Profe et al., 2016), shows only minor fluctuations in the entire lower section until SU 12. In contrast, significant decreases in ^{87}Sr/^{86}Sr and increases in εNd are observed within GS 7 (top of SU 6 and SU 7) towards GI 6 (SU 8) and GS 6 (on top of SU 8) towards GI 5.2 (SU 11), respectively.
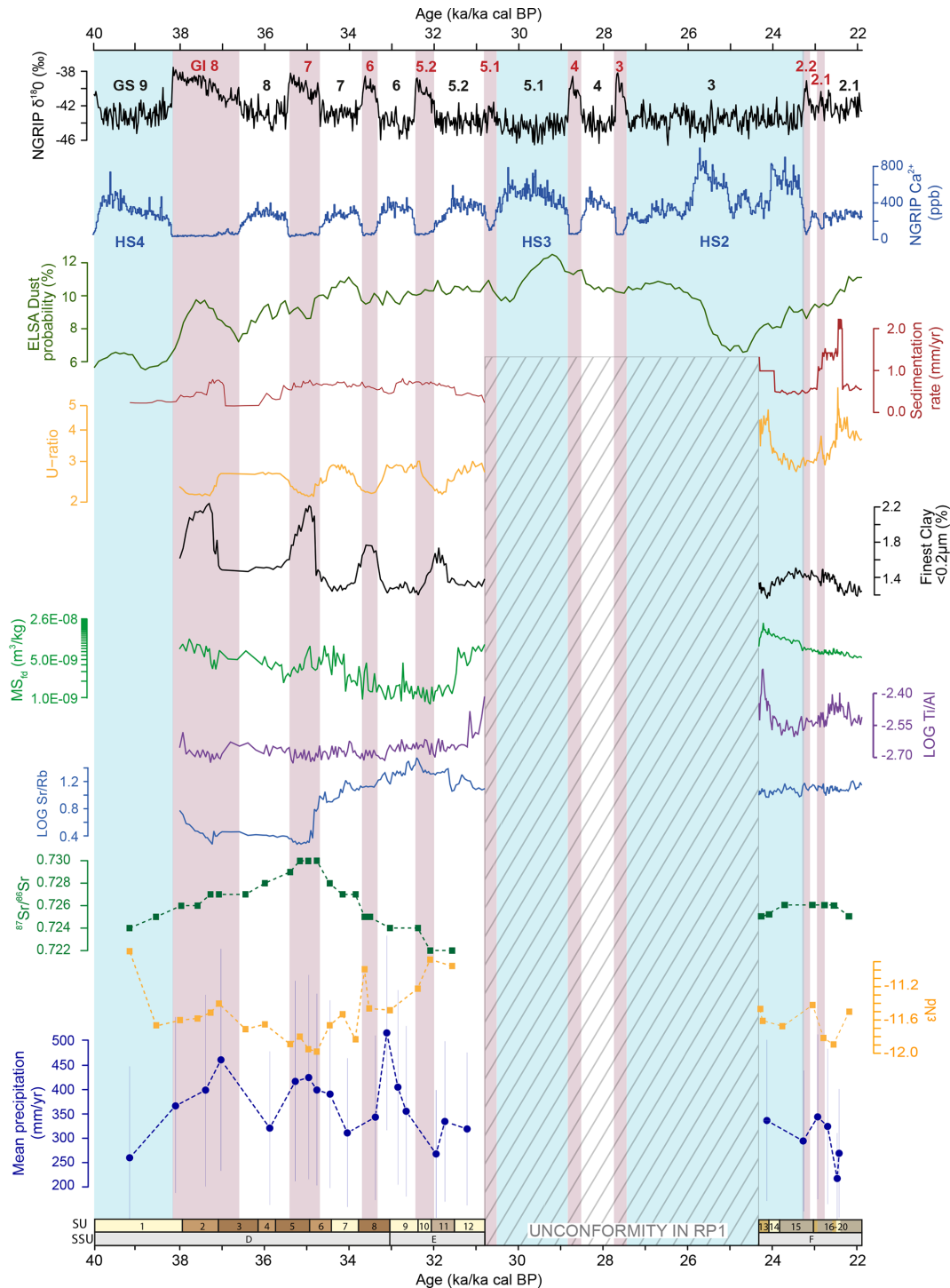
Figure 6. Comparison of selected proxy data from Schwalbenberg RP1, compared with the NGRIP event stratigraphy, with $\delta^{18}O$ and Ca^{2+} according to Rasmussen et al. (2014), and ELSA dust probability according to Seelos et al. (2009). Greenland Interstadials (GIs 8 to 2.1) are numbered in red and Greenland Stadials (GSs) in black, and Heinrich Stadials (HS4 to HS2) according to Reutenauer et al. (2015) are highlighted in light blue. Originally given as ages in years before 2000, the chronological scale has been shifted by 50 years to allow for direct comparisons with the calibrated radiocarbon scale given in calibrated years before CE 1950 (cal BP). Chronostratigraphy and sedimentation rates from Schwalbenberg are based on Bayesian age–depth modelling of the radiocarbon dated sequence using IntCal20 (cf. Prud'homme et al., 2022). U ratio, finest clay, frequency dependence of magnetic susceptibility MS_{fd} ($\Delta\chi$(fd)), log Ti/Al, and log SR/Rb are based on a continuous 2 cm sampling interval. $^{87}Sr/^{86}Sr$ and εNd are based on 35 samples along the profile (see Fig. 4). Mean annual precipitation estimates are based on the $\delta^{13}C$ values of ECGs (Prud'homme et al., 2022). SUs and SSUs according to Fischer et al. (2021). All data are given in Tables ST1 and ST2 in the Supplement.

These trends are likely to be related to a provenance change (see Sect. 5.2) that was contemporary with a strong decrease in reconstructed precipitation values.

During the following GS 5.2 a significant shift occurred. This was characterized by increased input of fine magnetic particles in accordance with a distinct increase in log Ti/Al and enhanced wind dynamics as indicated by the U ratio. In combination with the observed isotopic signals, this indicates severe changes in palaeoenvironmental conditions (see Sect. 5.3).

Above the unconformity, which we constrain to a hiatus of up to 6.5 kyr (between 30 800 and 24 300 cal BP), completely different characteristics are observed in both the stratigraphic record and the proxy data. We interpret the maxima in the U ratio, MS, and MS_{fd} as well as in log Ti/Al in SU 13 as the result of sediment relocation and recycling involving re-deposition of the Eltville tephra. The latter contains detrital volcanogenic magnetic Ti–Fe oxides which show frequently an oxidized rim of maghemite resulting from low-temperature oxidation upon incorporation into sediment. This oxidation process leads to particle-internal fining causing increasing superparamagnetic behaviour similar to pedogenic neo-formation. Here, it is limited to the maghemized shell consisting of ultrafine domains in the superparamagnetic single-domain (SD) range and therefore significantly increases the MS (e.g. Liu et al., 2012; Zhang et al., 2021). The highest sedimentation rates are in accordance with input of coarser material as indicated by the highest U ratio values. ELSA dust probability is also indicating increased dustiness, which is – for this time interval – not observed in NGRIP Ca^{2+}. The finest clay at RP1 is slightly increased where the U ratio forms a minimum related to the weakly developed Gelic Gleysols. After the distinct maximum, the MS_{fd} shows a continuous decrease. While log Sr/Rb and $^{87}Sr/^{86}Sr$ show almost no variations, log Ti/Al is increasing contemporarily with fluctuating εNd during GS 2, for which the lowest precipitation value is reconstructed. Overall, the stratigraphy and related proxy data and the comparison to NGRIP indicate that above the unconformity the dominance of local to regional effects caused the major changes.

5.2 Isotope geochemistry and AMS-derived near-surface wind trends: identification of dust source–sink relationships?

Potential shifts in dust provenance from the OIS 3 to OIS 2 transition have been reported based on bulk geochemistry and luminescence sensitivity for different Schwalbenberg LPSs (Klasen et al., 2015; Profe et al., 2016; Fitzsimmons et al., 2021; Vinnepand et al., 2022). These studies indicate that sediment recycling within local source areas as well as changes in wind direction may have caused the different signals. Here, we add information on isotopic composition and AMS-derived near-surface wind trends for Schwalbenberg RP1. We compare Sr and Nd isotope data from differ-

ent potential dust source areas in western Europe (Fig. 7a). As stated before (see Sects. 4.1, 5.1), the variations in εNd are restricted to a narrow range, and significant shifts in $^{87}Sr/^{86}Sr$ in the lower section of the sequence may be related to enhanced in situ weathering. Against this background, caution is required in interpreting the presented data, but, nevertheless, our combination of proxies allows for some substantial contributions to the discussion of dust source-to-sink relationships. This is especially true as data on dust provenance based on precisely dated LPSs are still rather scarce, with Schwalbenberg RP1 representing one of the best dated LPSs of the wider region (Prud'homme et al., 2022).

Overall, the relatively coarse character of the silt and the regional geographic setting of the Schwalbenberg at the confluence of the rivers Ahr and Rhine in the centre of the Rhenish Massif (Fig. 1) suggest dominating local to regional dust components in most parts of the RP1 profile. Figure 7 shows that the Schwalbenberg Sr and Nd isotope data generally plot along a gradient between the recent suspended sediment load of the Upper Rhine (Tricca et al., 1999) and Devonian slates from the Rhenish Massif (Moragues-Quiroga et al., 2017). Hence, both the Rhine catchment and the Rhenish Massif can be assumed as potential silt source areas. In addition, both mixing hyperbolas between Eifel volcanites and the Devonian slates and the Siebengebirge and Westerwald volcanites and the Devonian slates indicate a certain amount of these volcanites to the Schwalbenberg LPSs. This might also be reflected in the relatively high Nd concentrations at Schwalbenberg (mean: 68.48 ppm; $n = 30$) in comparison to the Rhine suspended sediment load (11.1 ppm; Tricca et al., 1999), the Devonian slates of the Rhenish Massif (mean: 44.39 ppm; $n = 5$; Moragues-Quiroga et al., 2017), and regional Pleistocene periglacial slope deposits (mean = 44.64 ppm; $n = 3$; Moragues-Quiroga et al., 2017). As reference, leucite basalt and phonolite andesites typically have high Nd concentrations around 81 ppm (Faure and Mensing, 2005).

In contrast to Schwalbenberg, the LPS key sections of Nussloch (Figs. 1, 7), located approx. 200 km south-southeast on the eastern bank of the Upper Rhine, appear to be dominated by dust input from the alluvial plain of the Rhine River and other local sources (Schatz et al., 2015).

For other LPSs like Kesselt and Rocourt, both situated in Belgium at the north-western edge of the Rhenish Massif (Fig. 1), Sr and Nd isotope values of sediments that were deposited within the LGM (Gallet et al., 1998) indicate an important role of the Rhenish Massif as an additional local dust source besides the Rhine system. Similar findings were also reported for OIS 2 loess within the southern part of the Lower Rhine Embayment and the north-western edge of the Rhenish Massif (northern edge of the Eifel area) by Janus (1988). In that study a systematic increase in heavy minerals indicative of short-distance transport from the Eifel and Rhenish Massif sediment source towards LPSs located north-west of Schwalbenberg was observed, next to heavy minerals indica-
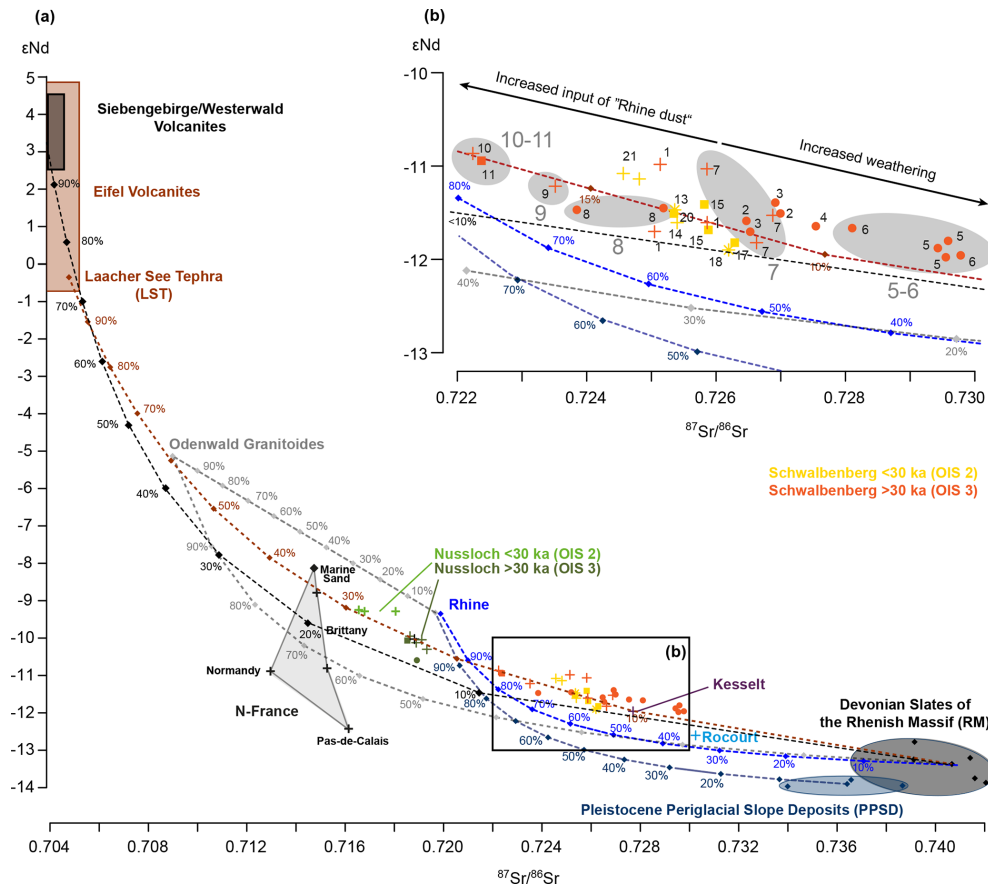
Figure 7. (a) εNd and ^{87}Sr/^{86}Sr of reference samples from different sites in western central Europe in comparison to Schwalbenberg RP1. Mixing hyperbolas indicate the possible mixing of two endmembers (in percentage) considering their Sr and Nd element concentrations and their respective isotope values (cf. Faure and Mensing, 2005; all data are presented in Table ST3 in the Supplement) and were calculated for mixtures between different endmembers (Devonian slate saprolite of the Rhenish Massif as continental crust endmember (grey; Moragues-Quiroga et al., 2017), Rhine suspended sediment load (blue; Tricca et al., 1999), Odenwald granitoids (light grey; Siebel et al., 2012), Siebengebirge and Westerwald volcanites (black; Schubert et al., 2015), Laacher See tephra and Eifel volcanites (red, as mantle-representing endmember; Wörner et al., 1985; note that Förster et al. (2020) showed that the Eltville tephra found at Schwalbenberg originated from an earlier eruption of the Laacher See volcano at 24.3 ka), northern France (Gallet et al., 1998), and Pleistocene periglacial slope deposits (PPSDs) in the Rhenish Massif (Moragues-Quiroga et al., 2017)). Our plot suggests that the Schwalbenberg LPSs are dominated by sediments from the Rhine valley as also described for Nussloch (Schatz et al., 2015). Compared to the latter, the isotope composition of the Kesselt and Rocourt LPSs (Gallet et al., 1998) (see Fig. 1) and the Schwalbenberg LPSs indicate a higher amount of dust originating from Devonian slates of the Rhenish Massif and/or PPSDs overlying the Devonian rocks. In addition, mantle-derived material from the Eifel and from the Siebengebirge and Westerwald potentially contributes to the dust deposited at Schwalbenberg. Odenwald granitoids may reflect a contribution via small Rhine tributaries. **(b)** Detail of plot **(a)** (see inset): the grey numbers refer to SUs, and the grey ellipses highlight that the samples above SU 7 up to SU 11 may reflect an enhanced contribution of sediments from the Rhine towards the end of OIS 3. In contrast, SUs below SU 7 down to SU 5, correlating to matured Calcaric Cambisols from the basal soil complex of the RP1 profile, plot offsite towards more radiogenic Sr isotope values, indicating enhanced weathering. Symbology: loess (+), reworked loess (∗), Gelic Gleysols (■), and Calcaric Cambisols (●).

tive of Rhine terraces and small Eifel riverbeds dissecting the Rhine terraces as the main source areas.

Although the data shown in Fig. 7 indicate general differences in dust provenance, we have to keep in mind that (i) the variations in Schwalbenberg RP1 Sr isotope composition are certainly also influenced by in situ pedogenesis (see Fig. 7b, especially within SUs 5 and 6 where the strongest weathering is observed); (ii) the reference data for the suspended sed-

iment load from the southernmost part of the Upper Rhine River (south of the Kaiserstuhl; see Fig. 1) mainly reflect material originating from Miocene marine sediments of the Alpine Molasse (Buhl et al., 1991), thus not including important Rhine tributaries located further north (e.g. the rivers Main, Nahe, Lahn, and Mosel); (iii) also non-alpine provenance spectra contribute considerably to the Pleistocene and recent sediment budged of the Upper Rhine (Preusser et al.,

2021; Hülscher et al., 2018); and (iv) sediments from the Rhine catchment most likely experienced several cycles of grain size reduction, sorting, and mixing within the alluvial plain and fluvial transport prior to its deposition at the Schwalbenberg LPSs. Such processes occurring in the alluvial plains of river systems have recently been discussed by Pötter et al. (2021) for LPSs from the Lower Danube and by Baykal et al. (2022) for LPSs from the northern fringe of the European loess belt in the context of dust provenance.

Despite the given limitations a clear change in isotope composition after GI 7 (top of SU 6 and SU 7) and after GI 6 (SU 8) up to GS 5.2 (top SU 11) is indicated by slightly increasing εNd and decreasing ^{87}Sr/^{86}Sr values, pointing to enhanced input of dust being more comparable to the Rhine suspended load (see Fig. 7b). This trend is accompanied by a reduction of fine magnetic particles (decreasing MS_{fd}), reduced weathering (increasing log Sr/Rb), and gustier winds indicated by a dominance of wind vigour (inverse behaviour of MS and MS_{fd}) and high U ratio values (see Sect. 5.1).

Throughout the upper section of RP1 both isotope ratios do not show typical inverse trends (Fig. 6). This may be due to sediment sorting and reworking as observed within the RP1 upper section, which may have biased the Sr isotope composition. Nevertheless, slightly varying εNd values in combination with significant variations in log Ti/Al might reflect increased dust input from local to regional sources of the Rhenish Massif. In combination with the AMS-based reconstruction of SSW–NNE near-surface wind trends (Figs. 4, 8), we assume that the alluvial plains of the rivers Rhine and Ahr most likely are the dominating local sediment sources for the investigated part of the Schwalbenberg LPS.

Based on our AMS data, however, we cannot decide whether the near-surface winds came from SSW or NNE, but wind regime statistics for the Schwalbenberg site in the valley setting indicate an overall dominance of westerly and south-westerly winds during the LGM and recent times (Prud'homme et al., 2022).

In addition to these large alluvial sources, exposed fine-grained rocks (e.g. in the incised upper Ahr valley), alluvial plains of small creeks, abandoned river terraces, and widespread Pleistocene periglacial slope deposits (PPSDs) may also have played an important role in silt production. Furthermore, recycling of loess deposits may have contributed an additional dust component into the LPS (cf. Mroczek, 2013).

Overall, the obtained data on dust provenance and near-surface wind trends point to dominating local dust sources that were associated with gustier winds with predominant SSW–NNE wind directions in stadial phases, while interstadials may have been characterized by a significant dust component from more distant sources. In this context, we found a significant negative relationship between the AMS foliation (F) and the U ratio in SUs 5, 7, and 8 (see Fig. S4), whereof SU 5 correlates to GI 7 and SU 8 to GI 6 (Fig. 6). This may indicate that fine to medium silt particles establish
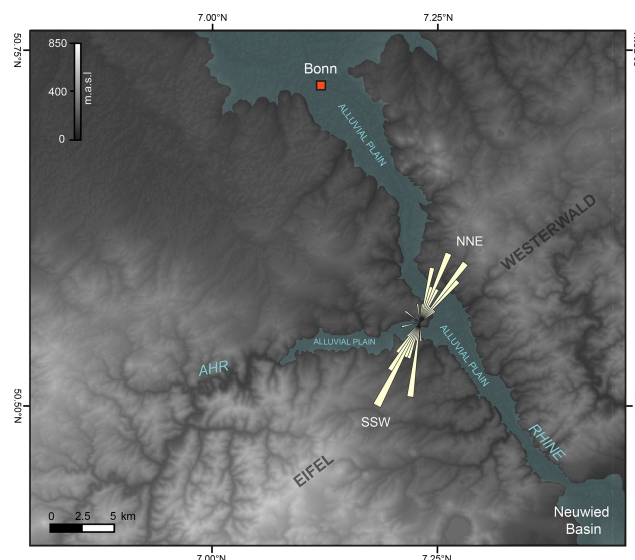

Figure 8. DEM-based map (SRTM 30; USGS 2022) showing reconstructed near-surface wind trends for the Schwalbenberg site and possible short distance entrainment areas for mineral dust. The SSW–NNE wind trend estimates are only based on AMS measurements of loess samples (beige rose diagram), which passed the assessment protocol for primary magnetic fabric (see Fig. 4) that is described in Sects. 3.3 and S1. For AMS stereoplots and rose diagrams please see Fig. 5.

the AMS signal within these interstadials, possibly owing to the continuous accumulation of dust during soil formation resulting in accretionary palaeosols (Fischer et al., 2021; Vinnepand et al., 2022). To our knowledge, such a clear correlation between finer grain sizes and increasing foliation has been so far not described in any LPS on stadial–interstadial scales (cf. Bradák et al., 2021). However, Zhang et al. (2010) proposed a model in which more frequent summer precipitation during relative mild climatic periods (interglacials and interstadials) led to an improved settling of anisotropic grains (e.g. micas and clay minerals), causing the overall increased AMS foliation. In contrast, most loess units throughout RP1 and weakly developed Gelic Gleysols in the upper section (SUs 15, 17, 20) show a positive linear relationship between F and the U ratio, indicating that coarse silt particles play a major role for the AMS signal in these units that were related to gustier winds and input of short-travelled dust.

5.3 Palaeoenvironmental and palaeoclimatic implications

Millennial- to centennial-scale synchronicity between the Schwalbenberg LPSs and the NGRIP δ^{18}O record was proposed based on litho- and pedostratigraphic evidence combined with organic carbon contents (Fischer et al., 2021), further attested by radiocarbon dating and a quantitative climate reconstruction based on the investigation of ECGs (Prud'homme et al., 2022). Here we observe very largely

synchronous patterns between NGRIP $\delta^{18}O$ and Ca^{2+} and the Schwalbenberg sedimentological proxies (U ratio, finest clay), further supporting the close synchronicity of western European and North Atlantic climate changes. In addition, we present proxy data allowing for further characterization of the dust deposited within the Schwalbenberg LPSs and comprehensive palaeoenvironmental reconstructions based on magnetic fabric, environmental magnetism, bulk geochemistry, and isotope composition.

The lower section of the Schwalbenberg RP1 profile covers in high resolution the period from the end of GS 9 (contemporary with Heinrich Stadial 4) to the end of GS 5.2 (Fig. 6). In the wider region this period is characterized by a distinct opening of the landscape as suggested by a landscape evolution model of the Eifel area that is based on multi-method approaches applied to ELSA (Sirocko et al., 2016). This model documents the transition from boreal forested environments (landscape evolution zone (LEZ) 7, onset ∼ 49 years b2k) to steppe-like open environments (LEZ 6, ∼ 36.4–28.45 years b2k), which is interpreted as the environmental reaction due to a longer cooling trend accompanied by increased aridity in the Rhenish Massif at roughly the time of the OIS 3 to OIS 2 transition. At Schwalbenberg this cooling trend is, on the one hand, reflected in decreasing intensities of soil formation from the lower soil complex (SUs 2–6, covering GI 8 and 7) towards the Calcaric Cambisol correlated to GI 6 (SU 8) and the Gelic Gleysol correlated to GI 5 (SU 11) (cf. Vinnepand et al., 2020; Fischer et al., 2021). On the other hand, overall increasing U ratio values and the reduction of fine magnetic particles as indicated by decreasing MS_{fd} values point towards an enhancement of wind activity and increasing dryness simultaneously with reduced sediment recycling until mid-GS 5.2 at ∼ 31 500 cal BP. The latter is also supported by reduced weathering intensity following GI 7, as evidenced in a slightly increasing log Sr/Rb ratio accompanied by a distinct decrease in $^{87}Sr/^{86}Sr$ and an increase in εNd. This can be interpreted in terms of an enhanced input of dust that carries an isotope signal comparable to that of the Rhine's suspended load (Fig. 7b). This trend coincides with distinct aridification, climate cooling, and grain coarsening observed in some LPSs along the Rhine during late OIS 3 (Prud'homme et al., 2018; Vinnepand et al., 2020) and might be related to intensified periglacial conditions in the local silt sources and enhanced glacial grinding activity and sediment availability in front of the advancing Alpine ice sheet and the Rhine Glacier in particular (Ivy-Ochs et al., 2008).

For the interstadial periods we are able to reconstruct reduced but still pronounced dust deposition at the Schwalbenberg LPSs (Fischer et al., 2021; Prud'homme et al., 2022). Vegetation cover and moister conditions as suggested by Prud'homme et al. (2022) especially for GIs 8–6 for Schwalbenberg favour (reduced) dust deposition rather than its entrainment (see Újvári et al., 2016). In addition, intensified syn-sedimentary soil formation in interstadials, especially

during GI 8 and GI 7, leads to the production of clay minerals in the course of silicate weathering, hampering the entrainment of particles due to strong cohesion and adhesion forces (cf. Újvári et al., 2016). As discussed before, we observed an inverse correlation of the U ratio and the AMS foliation but a positive correlation of the finest clay and the foliation within the Calcaric Cambisols of the lower section of RP1 (see Sect. S1). This could point, beside secondary grain size reduction in the course of pedogenesis, to an input of finer-grained (potentially long-distant) aeolian material during interstadials, which might be also visible in described shifts in εNd (see Sect. 5.2).

At Schwalbenberg we observe a further distinct shift around 31 500 cal BP associated with increased wind activity and in particular significantly enhanced sediment recycling reflected by a distinct shift in MS_{fd} and a potential provenance shift indicated by log Ti/Al (Fig. 6). On a regional scale, the same period is characterized by increased flood activity in the Eifel area (Sirocko et al., 2016) possibly related to enhanced seasonal landscape instability caused by a reduced vegetation cover and associated sediment relocation. On a supra-regional scale, the advancing Fennoscandian (FIS) and British–Irish ice sheets (BIIS) correlating with the onset of the LGM (Lambeck et al., 2014), with some moderate ice marginal retreats during HS3 (Toucanne et al., 2015), and the further advancing Rhine Glacier (Ivy-Ochs et al., 2008) played an important role in dust production and circulation patterns in western, central, and eastern Europe (Schaffernicht et al., 2020). Simultaneously, a significant increase in the sedimentation rate occurred at Nussloch (Prud'homme et al., 2022), whereas in northern France the first genuine loess unit originates only from the following stadial GS 5.1 (Antoine et al., 2014). Associated with overall cooler and drier conditions over western and central Europe during the LGM, evidence is provided for cyclones that were capable of triggering enhanced dustiness related to higher wind speeds (Pinto and Ludwig, 2020). This is in agreement with the assumption of strong NW winds especially between 34 and 17 ka, resulting in local input of coarse aeolian material, high sedimentation rates, and the SE-trending "greda" morphology at Nussloch (Antoine et al., 2009).

At Schwalbenberg RP1, however, on top of the distinct unconformity that is related to local channel formation and sediment relocation, which may have reworked and included the Eltville tephra (Fischer et al., 2021), different proxies pinpoint environmental conditions that were significantly different from the preceding ones that were most likely dominated by local to regional signals.

Sediment relocation reflected within SU 13 was followed by reduced wind activity, input of finer-grained sediments, and reduced sedimentation rates until ∼ 22 900 cal BP, roughly coinciding with the later part of LEZ 5 in the Eifel area that represents the transition from steppe to tundra-like environments (Sirocko et al., 2016).

After 22 900 cal BP, the sedimentation rate and U ratio reach the highest values throughout the entire RP1 profile, indicating increased dustiness but also potential sediment reworking processes. Enhanced dustiness is, however, also reflected in the REM 3 LPS (cf. Fischer et al., 2021; Fig. 3) and the ELSA dust probability (Fig. 6) associated with the development of the polar desert of LEZ 4 in the Eifel area (Sirocko et al., 2016) but is decoupled from NGRIP Ca^{2+}, which shows a clear minimum after 23 300 BP.

Further evidence for local to regional dust transport is provided by heavy mineral analyses of the Dehner Maar, where increased dust activity and a shift from predominantly westerly to strong easterly winds is reported for the period from 23 until 20 ka (Römer et al., 2016). In this context, the AMS-based reconstruction of near-surface wind trends at Schwalbenberg RP1 may point to periods with significant north-easterly winds during overall dominating western wind directions (Prud'homme et al., 2022). This would be in agreement with dust-cycle simulations for the LGM, showing that beside westerlies and embedded cyclones persistent easterlies associated with anticyclonic flow may have also played a significant role for dust deposition. These would have resulted in westward-running dust plumes and associated high dust accumulation rates in the North German plain including adjacent regions (Pinto and Ludwig, 2020; Schaffernicht et al., 2020).

6 Conclusions

We present an integrative approach that systematically combines physical and geochemical proxies, enabling a synthetic interpretation of LPS formation in western central Europe. We focus on the Schwalbenberg RP1 LPS that is exposed north-west of the confluence of the Ahr and Rhine rivers in the centre of the Rhenish Massif. We integrate our data into a robust and reliable age model that has been established based on high-resolution dating of ECGs. We show that Schwalbenberg RP1 is subdivided into a lower section and an upper section that are separated by a major stratigraphic unconformity. Whereas the lower section corresponds to late OIS 3 ($\sim$ 39 200–30 800 cal BP; end of GS 9 until GS 5.2), the upper section dates into the LGM ($\sim$ 24 300–21 900 cal BP; end of GS 3 until GS 2.1).

In general, we could confirm the assumption of synsedimentary soil formation during interstadials, give evidence for provenance changes with overall dominating local to regional dust sources, and confirm the close temporal linkages to other climate archives in the North Atlantic region, which we have highlighted in earlier studies.

Based on our synthetic approach we can draw the following, more specific conclusions:

- In combination with the established age model, the sedimentological proxies of the lower section at Schwalbenberg RP1 attest to – to a certain degree – simi-

lar and largely synchronous patterns of northern hemispheric climatic changes as evidenced in NGRIP $\delta^{18}O$ and Ca^{2+}, supporting the overall synchronicity of climatic changes in and around the North Atlantic region.

- A significant negative relationship between the AMS foliation and the U ratio found in interstadial palaeosols and intercalated stadial loess layers, respectively, may indicate that fine to medium silt particles increase the foliation. This could possibly reflect the continuous accumulation of fine dust during soil formation and the simultaneous increase in precipitation, causing improved alignment of sediment grains into the bedding plain. To our knowledge, such a clear correlation between finer grain size and increasing foliation has so far not been described for any LPS for stadial–interstadial cycles, i.e. on millennial to centennial timescales.

- A distinct shift towards increased input of "Rhine dust" and reduced weathering intensity occurs simultaneously with an overall cooling and aridification trend in Europe towards the end of OIS 3.

- A further distinct shift visible in all proxy data around 31 500 cal BP, interpreted in terms of enhanced wind activity with significant input of coarse-grained material recycled from local sources, is possibly related to increased landscape instability when tundra-like conditions – probably associated with deep seasonal or even permafrost – developed towards the LGM.

- The proxies within the upper section pinpoint environmental conditions that were significantly different from those in the lower section, which were most likely dominated by more local to regional signals and high sedimentation rates.

- AMS-based reconstructions of near-surface wind trends may indicate the influence of north-easterly winds beside the overall dominance of westerlies and embedded cyclones, causing high dust accumulation rates.

Overall, by integrating our approach in the study of LPSs over a broader geographic area, we see the opportunity for a more comprehensive understanding of LPS formation including changes in dust composition and associated circulation patterns during Quaternary climate changes.

References

Antoine, P., Rousseau, D.-D., Moine, O., Kunesch, S., Hatté, C., Lang, A., Tissoux, H., and Zöller, L.: Rapid and cyclic aeolian deposition during the Last Glacial in European loess: a high-resolution record from Nussloch, Germany, Quaternary Sci. Rev., 28, 2955–2973, https://doi.org/10.1016/j.quascirev.2009.08.001, 2009.

Antoine, P., Goval, E., Jamet, G., Coutard, S., Moine, O., Hérisson, D., Auguste, P., Guérin, G., Lagroix, F., Schmidt, E., Robert, V., Debenham, N., Meszner, S., and Bahain, J. J.: The upper pleistocene loess sequences of havrincourt (Pas-de-Calais, France). Stratigraphy, palaeoenvironments, geochronology and human occupations, Quaternaire, 25, 321–368, https://doi.org/10.4000/quaternaire.7278, 2014.

Baykal, Y., Stevens, T., Bateman, M. D., Pfaff, K., Sechi, D., Banak, A., Šuica, S., Zhang, H., and Nie, J.: Eurasian Ice Sheet derived meltwater pulses and their role in driving atmospheric dust activity: Late Quaternary loess sources in SE England, Quaternary Sci. Rev., 296, 107804, https://doi.org/10.1016/j.quascirev.2022.107804, 2022.

Blaauw, M. and Christeny, J. A.: Flexible paleoclimate age-depth models using an autoregressive gamma process, Bayesian Anal., 6, 457–474, https://doi.org/10.1214/11-BA618, 2011.

Blott, S. J., Croft, D. J., Pye, K., Saye, S. E., and Wilson, H. E.: Particle size analysis by laser diffraction, Geological Society, London, Special Publications, 232, 63–73, https://doi.org/10.1144/GSL.SP.2004.232.01.08, 2004.

Boenigk, W. and Frechen, M.: The Pliocene and Quaternary fluvial archives of the Rhine system, Quaternary Sci. Rev., 25, 550–574, https://doi.org/10.1016/j.quascirev.2005.01.018, 2006.

Bradák, B., Seto, Y., Chadima, M., Kovács, J., Tanos, P., Újvári, G., and Hyodo, M.: Magnetic fabric of loess and its significance in Pleistocene environment reconstructions, Earth-Sci. Rev., 210, 103385, https://doi.org/10.1016/j.earscirev.2020.103385, 2020.

Bradák, B., Seto, Y., Stevens, T., Újvári, G., Fehér, K., and Költringer, C.: Magnetic susceptibility in the European Loess Belt: New and existing models of magnetic enhancement in loess, Palaeogeogr. Palaeocl., 569, 110329, https://doi.org/10.1016/j.palaeo.2021.110329, 2021.

Buggle, B., Glaser, B., Hambach, U., Gerasimenko, N., and Marković, S.: An evaluation of geochemical weathering indices in loess-paleosol studies, Quaternary Int., 240, 12–21, https://doi.org/10.1016/j.quaint.2010.07.019, 2011.

Buggle, B., Hambach, U., Müller, K., Zöller, L., Marković, S. B., and Glaser, B.: Iron mineralogical proxies and quaternary climate change in SE-european loess-paleosol sequences, Catena, 117, 4–22, https://doi.org/10.1016/j.catena.2013.06.012, 2014.

Buhl, D., Neuser, R. D., Richter, D. K., Riedel, D., Roberts, B., Strauss, H., and Veizer, J.: Nature and nurture: Environmental isotope story of the River Rhine, Naturwissenschaften, 78, 337–346, https://doi.org/10.1007/BF01131605, 1991.

Clauer, N. and Chaudhuri, S.: Clays in Crustal Environments, Springer, Berlin, Heidelberg, https://doi.org/10.1007/978-3-642-79085-0, 1995.

DePaolo, D. J. and Wasserburg, G. J.: Nd isotopic variations and petrogenetic models, Geophys. Res. Lett., 3, 249–252, https://doi.org/10.1029/GL003i005p00249, 1976.

Deutscher Wetterdienst: Deutscher Wetterdienst (German Meteorological Service): https://www.dwd.de/DE/leistungen/klimadatendeutschland/klimadatendeutschland.html, (last access: 2 March 2022), 2023.

Drouet, Th., Herbauts, J., Gruber, W., and Demaiffe, D.: Natural strontium isotope composition as a tracer of weathering patterns and of exchangeable calcium sources in acid leached soils developed on loess of central Belgium, Eur. J. Soil Sci., 58, 302–319, https://doi.org/10.1111/j.1365-2389.2006.00840.x, 2007.

Evans, M. E. and Heller, F.: Magnetism of loess/palaeosol sequences: recent developments, Earth-Sci. Rev., 54, 129–144, https://doi.org/10.1016/S0012-8252(01)00044-7, 2001.

Evans, M. E. and Heller, F.: Environmental Magnetism: Principles and Applications of Enviromagnetics, Elsevier, Amsterdam, 318 pp., ISBN 978-0-122-43851-6, 2003.

Faure, G. and Mensing, T. M.: Principles and applications, John Wiley & Sons, Inc, New York, ISBN 978-0-471-38437-3, 2005.

Federal Institute for Geosciences and Natural Resources Germany: Federal Institute for Geosciences and Natural Resources Germany, https://www.bgr.bund.de/DE/Home/homepage_node.html, last access: 23 March 2022.

Feng, J.-L., Zhu, L.-P., Zhen, X.-L., and Hu, Z.-G.: Grain size effect on Sr and Nd isotopic compositions in eolian dust: implications for tracing dust provenance and Nd model age, Geochem. J., 43, 123–131, https://doi.org/10.2343/geochemj.1.0007, 2009.

Fischer, P., Hambach, U., Klasen, N., Schulte, P., Zeeden, C., Steininger, F., Lehmkuhl, F., Gerlach, R., and Radtke, U.: Landscape instability at the end of MIS 3 in western Central Europe: evidence from a multi proxy study on a Loess-Palaeosol-Sequence from the eastern Lower Rhine Embayment, Germany, Quaternary Int., 502, 119–136, https://doi.org/10.1016/j.quaint.2017.09.008, 2019.

Fischer, P., Jöris, O., Fitzsimmons, K. E., Vinnepand, M., Prud'homme, C., Schulte, P., Hatté, C., Hambach, U., Lindauer, S., Zeeden, C., Peric, Z., Lehmkuhl, F., Wunderlich, T., Wilken, D., Schirmer, W., and Vött, A.: Millennial-scale terrestrial ecosystem responses to Upper Pleistocene climatic changes: 4D-reconstruction of the Schwalbenberg Loess-Palaeosol-Sequence (Middle Rhine Valley, Germany), CATENA, 196, 104913, https://doi.org/10.1016/j.catena.2020.104913, 2021.

Fitzsimmons, K. E., Perić, Z., Nowatzki, M., Lindauer, S., Vinnepand, M., Prud'homme, C., Dave, A. K., Vött, A., and Fischer, P.: Luminescence Sensitivity of Rhine Valley Loess: Indicators of Source Variability?, Quaternary, 5, 1, https://doi.org/10.3390/quat5010001, 2021.

Förster, M. W., Zemlitskaya, A., Otter, L. M., Buhre, S., and Sirocko, F.: Late Pleistocene Eifel eruptions: insights from clinopyroxene and glass geochemistry of tephra layers from Eifel Laminated Sediment Archive sediment cores, J. Quaternary Sci., 35, 186–198, https://doi.org/10.1002/jqs.3134, 2020.

Forster, Th., Evans, M. E., and Heller, F.: The frequency dependence of low field susceptibility in loess sediments, Geophys. J. Int., 118, 636–642, https://doi.org/10.1111/j.1365-246X.1994.tb03990.x, 1994.

Frechen, M., Oches, E., and Kohlfeld, K.: Loess in Europe – mass accumulation rates during the Last Glacial Period, Quaternary Sci. Rev., 22, 1835–1857, https://doi.org/10.1016/S0277-3791(03)00183-5, 2003.

Fuhrmann, F., Seelos, K., and Sirocko, F.: Eolian sedimentation in central European Auel dry maar from 60 to 13 ka, Quaternary Res., 101, 4-12, https://doi.org/10.1017/qua.2020.81, 2021.

Gallet, S., Jahn, B., Van Vliet Lanoë, B., Dia, A., and Rossello, E.: Loess geochemistry and its implications for particle origin and composition of the upper continental crust, Earth Planet. Sci. Lett., 156, 157–172, https://doi.org/10.1016/S0012-821X(97)00218-5, 1998.

Goldstein, S. J. and Jacobsen, S. B.: The Nd and Sr isotopic systematics of river-water dissolved material: Implications for the sources of Nd and Sr in seawater, Chem. Geol.: Isotope Geoscience section, 66, 245–272, https://doi.org/10.1016/0168-9622(87)90045-5, 1987.

Goldstein, S. J. and Jacobsen, S. B.: Nd and Sr isotopic systematics of river water suspended material: implications for crustal evolution, Earth Planet. Sci. Lett., 87, 249–265, https://doi.org/10.1016/0012-821X(88)90013-1, 1988.

Goldstein, S. L., O'Nions, R. K., and Hamilton, P. J.: A Sm-Nd isotopic study of atmospheric dusts and particulates from major river systems, Earth Planet. Sci. Lett., 70, 221–236, https://doi.org/10.1016/0012-821X(84)90007-4, 1984.

Grousset, F. E. and Biscaye, P. E.: Nd and Sr Isotopes as Tracers of Wind Transport: Atlantic Aerosols and Surface Sediments, in: Paleoclimatology and Paleometeorology: Modern and Past Patterns of Global Atmospheric Transport, edited by: Leinen, M. and Sarnthein, M., Springer Netherlands, Dordrecht, 385–400, https://doi.org/10.1007/978-94-009-0995-3_16, 1989.

Grousset, F. E. and Biscaye, P. E.: Tracing dust sources and transport patterns using Sr, Nd and Pb isotopes, Chem. Geol., 222, 149–167, https://doi.org/10.1016/J.CHEMGEO.2005.05.006, 2005.

Hrouda, F.: Anisotropy of magnetic susceptibility of rocks in the Rayleigh Law region: Modelling errors arising from linear fit to non-linear data, Studia Geophyssica et Geodaetica, 51, 423–438, https://doi.org/10.1007/s11200-007-0024-5, 2007.

Hülscher, J., Bahlburg, H., and Pfänder, J.: New geochemical results indicate a non-alpine provenance for the Alpine Spectrum (epidote, garnet, hornblende) in quaternary Upper Rhine sediment, Sediment. Geol., 375, 134–144, https://doi.org/10.1016/j.sedgeo.2018.02.010, 2018.

Ivy-Ochs, S., Kerschner, H., Reuther, A., Preusser, F., Heine, K., Maisch, M., Kubik, P. W., and Schlüchter, C.: Chronology of the last glacial cycle in the European Alps, J. Quaternary Sci., 23, 559–573, https://doi.org/10.1002/jqs.1202, 2008.

Janus, U.: Löss der südlichen niederrheinischen Bucht, Kölner Geographische Arbeiten, 49, ISSN 0454-1294. 1988.

Jones, R. M.: Particle size analysis by laser diffraction: ISO 13320, standard operating procedures, and Mie theory, American Laboratory, Corpus ID 221270121, 2003.

Kämpf, L., Rius, D., Duprat-Oualid, F., Crouzet, C., and Millet, L.: Evidence for wind patterns and associated landscape response in Western Europe between 46 and 16 ka cal. BP, Quaternary Sci. Rev., 298, 107846, https://doi.org/10.1016/j.quascirev.2022.107846, 2022.

Klasen, N., Fischer, P., Lehmkuhl, F., and Hilgers, A.: Luminescence dating of loess deposits from the Remagen-Schwalbenberg site, Western Germany, Geochronometria, 42, 67–77, https://doi.org/10.1515/geochr-2015-0008, 2015.

Knippertz, P. and Stuut, J.-B. W. (Eds.): Mineral Dust, Springer Netherlands, Dordrecht, https://doi.org/10.1007/978-94-017-8978-3, 2014.

Lambeck, K., Rouby, H., Purcell, A., Sun, Y., and Sambridge, M.: Sea level and global ice volumes from the Last Glacial Maximum to the Holocene, P. Natl. Acad. Sci. USA, 111, 15296–15303, https://doi.org/10.1073/pnas.1411762111, 2014.

Lehmkuhl, F., Nett, J. J., Pötter, S., Schulte, P., Sprafke, T., Jary, Z., Antoine, P., Wacha, L., Wolf, D., Zerboni, A., Hošek, J., Marković, S. B., Obreht, I., Sümegi, P., Veres, D., Zeeden, C., Boemke, B., Schaubert, V., Viehweger, J., and Ham-

bach, U.: Loess landscapes of Europe – Mapping, geomorphology, and zonal differentiation, Earth-Sci. Rev., 215, 103496, https://doi.org/10.1016/j.earscirev.2020.103496, 2021.

Liu, Q., Roberts, A. P., Larrasoaña, J. C., Banerjee, S. K., Guyodo, Y., Tauxe, L., and Oldfield, F.: Environmental magnetism: Principles and applications, Rev. Geophys., 50, RG4002, https://doi.org/10.1029/2012RG000393, 2012.

Mahowald, N. M., Muhs, D. R., Levis, S., Rasch, P. J., Yoshioka, M., Zender, C. S., and Luo, C.: Change in atmospheric mineral aerosols in response to climate: Last glacial period, preindustrial, modern, and doubled carbon dioxide climates, J. Geophys. Res.-Atmos., 111, D10202, https://doi.org/10.1029/2005JD006653, 2006.

Marx, S. K., Kamber, B. S., McGowan, H. A., Petherick, L. M., McTainsh, G. H., Stromsoe, N., Hooper, J. N., and May, J.-H.: Palaeo-dust records: A window to understanding past environments, Global Planet. Change, 165, 13–43, https://doi.org/10.1016/j.gloplacha.2018.03.001, 2018.

McGee, D., Broecker, W. S., and Winckler, G.: Gustiness: The driver of glacial dustiness?, Quaternary Sci. Rev., 29, 2340–2350, https://doi.org/10.1016/j.quascirev.2010.06.009, 2010.

Meijs, E., Mücher, H., Ouwerkerk, G., Romein, A., and Stoltenberg, H.: Evidence of Presence of the Eltville Tuff Layer in Dutsch and Belgian Limbourg and the Consequences for the Loess Stratigraphy, E&G Quaternary Sci. J., 33, 59–78, https://doi.org/10.3285/eg.33.1.06, 1983.

Meschede, M.: Geologie Deutschlands: ein prozessorientierter Ansatz, Springer Spektrum, Berlin, 252 pp., ISBN 978-3662452974, 2018.

Meyer, R., Nicoll, G. R., Hertogen, J., Troll, V. R., Ellam, R. M., and Emeleus, C. H.: Trace element and isotope constraints on crustal anatexis by upwelling mantle melts in the North Atlantic Igneous Province: an example from the Isle of Rum, NW Scotland, Geol. Magazine, 146, 382–399, https://doi.org/10.1017/S0016756809006244, 2009.

Meyer, W. and Stets, J.: Das Rheintal zwischen Bingen und Bonn, Borntraeger, Berlin, 386 pp., ISBN 978-3-443-15069-3, 1996.

Moine, O., Antoine, P., Hatté, C., Landais, A., Mathieu, J., Prud'homme, C., and Rousseau, D. D.: The impact of Last Glacial climate variability in west-European loess revealed by radiocarbon dating of fossil earthworm granules, P. Natl. Acad. Sci. USA, 114, 209–214, https://doi.org/10.1073/pnas.1614751114, 2017.

Moragues-Quiroga, C., Juilleret, J., Gourdol, L., Pelt, E., Perrone, T., Aubert, A., Morvan, G., Chabaux, F., Legout, A., Stille, P., and Hissler, C.: Genesis and evolution of regoliths: Evidence from trace and major elements and Sr-Nd-Pb-U isotopes, CATENA, 149, 185–198, https://doi.org/10.1016/j.catena.2016.09.015, 2017.

Mroczek, P.: Recycled loesses – A micromorphological approach to the determination of local source areas of Weichselian loess, Quaternary Int., 296, 241–250, https://doi.org/10.1016/j.quaint.2013.02.040, 2013.

Muhs, D. R.: The geologic records of dust in the quaternary, Aeolian Res., 9, 3–48, https://doi.org/10.1016/j.aeolia.2012.08.001, 2013.

Obreht, I., Zeeden, C., Hambach, U., Veres, D., Marković, S. B., Bösken, J., Svirčev, Z., Bačević, N., Gavrilov, M. B., and Lehmkuhl, F.: Tracing the influence of Mediterranean climate on Southeastern Europe during the past 350,000 years, Sci. Rep., 6, 36334, https://doi.org/10.1038/srep36334, 2016.

Ozer, M., Orhan, M., and Isik, N. S.: Effect of Particle Optical Properties on Size Distribution of Soils Obtained by Laser Diffraction, Environ. Eng. Geosci., 16, 163–173, https://doi.org/10.2113/gseegeosci.16.2.163, 2010.

Pinto, J. G. and Ludwig, P.: Extratropical cyclones over the North Atlantic and western Europe during the Last Glacial Maximum and implications for proxy interpretation, Clim. Past, 16, 611–626, https://doi.org/10.5194/cp-16-611-2020, 2020.

Pötter, S., Veres, D., Baykal, Y., Nett, J. J., Schulte, P., Hambach, U., and Lehmkuhl, F.: Disentangling Sedimentary Pathways for the Pleniglacial Lower Danube Loess Based on Geochemical Signatures, Front. Earth Sci., 9, 600010, https://doi.org/10.3389/feart.2021.600010, 2021.

Preusser, F., Büschelberger, M., Kemna, H. A., Miocic, J., Mueller, D., and May, J.-H.: Exploring possible links between Quaternary aggradation in the Upper Rhine Graben and the glaciation history of northern Switzerland, Int. J. Earth Sci. (Geol. Rundsch), 110, 1827–1846, https://doi.org/10.1007/s00531-021-02043-7, 2021.

Profe, J., Zolitschka, B., Schirmer, W., Frechen, M., and Ohlendorf, C.: Geochemistry unravels MIS 3/2 paleoenvironmental dynamics at the loess–paleosol sequence Schwalbenberg II, Germany, Palaeogeogr. Palaeoclim. Palaeoecol., 459, 537–551, https://doi.org/10.1016/j.palaeo.2016.07.022, 2016.

Prud'homme, C., Lécuyer, C., Antoine, P., Hatté, C., Moine, O., Fourel, F., Amiot, R., Martineau, F., and Rousseau, D.-D.: $\delta^{13}C$ signal of earthworm calcite granules: A new proxy for palaeoprecipitation reconstructions during the Last Glacial in western Europe, Quaternary Sci. Rev., 179, 158–166, https://doi.org/10.1016/j.quascirev.2017.11.017, 2018.

Prud'homme, C., Fischer, P., Jöris, O., Gromov, S., Vinnepand, M., Hatté, C., Vonhof, H., Moine, O., Vött, A., and Fitzsimmons, K. E.: Millennial-timescale quantitative estimates of climate dynamics in central Europe from earthworm calcite granules in loess deposits, Commun. Earth Environ., 3, 1–14, https://doi.org/10.1038/s43247-022-00595-3, 2022.

Rasmussen, S. O., Bigler, M., Blockley, S. P., Blunier, T., Buchardt, S. L., Clausen, H. B., Cvijanovic, I., Dahl-Jensen, D., Johnsen, S. J., Fischer, H., Gkinis, V., Guillevic, M., Hoek, W. Z., Lowe, J. J., Pedro, J. B., Popp, T., Seierstad, I. K., Steffensen, J. P., Svensson, A. M., Vallelonga, P., Vinther, B. M., Walker, M. J. C., Wheatley, J. J., and Winstrup, M.: A stratigraphic framework for abrupt climatic changes during the Last Glacial period based on three synchronized Greenland ice-core records: refining and extending the INTIMATE event stratigraphy, Quaternary Sci. Rev., 106, 14–28, https://doi.org/10.1016/j.quascirev.2014.09.007, 2014.

Reimer, P. J., Austin, W. E. N., Bard, E., Bayliss, A., Blackwell, P. G., Bronk Ramsey, C., Butzin, M., Cheng, H., Edwards, R. L., Friedrich, M., Grootes, P. M., Guilderson, T. P., Hajdas, I., Heaton, T. J., Hogg, A. G., Hughen, K. A., Kromer, B., Manning, S. W., Muscheler, R., Palmer, J. G., Pearson, C., Van Der Plicht, J., Reimer, R. W., Richards, D. A., Scott, E. M., Southon, J. R., Turney, C. S. M., Wacker, L., Adolphi, F., Büntgen, U., Capano, M., Fahrni, S. M., Fogtmann-Schulz, A., Friedrich, R., Köhler, P., Kudsk, S., Miyake, F., Olsen, J., Reinig, F., Sakamoto, M., Sookdeo, A., and Talamo, S.: The IntCal20 Northern Hemisphere Radiocarbon Age Calibration Curve (0–55 cal kBP), Radiocarbon, 62, 725–757, https://doi.org/10.1017/RDC.2020.41, 2020.

Reutenauer, C., Landais, A., Blunier, T., Bréant, C., Kageyama, M., Woillez, M.-N., Risi, C., Mariotti, V., and Braconnot, P.: Quantifying molecular oxygen isotope variations during a Heinrich stadial, Clim. Past, 11, 1527–1551, https://doi.org/10.5194/cp-11-1527-2015, 2015.

Römer, W., Lehmkuhl, F., and Sirocko, F.: Late Pleistocene aeolian dust provenances and wind direction changes reconstructed by heavy mineral analysis of the sediments of the Dehner dry maar (Eifel, Germany), Global Planet. Change, 147, 25–39, https://doi.org/10.1016/j.gloplacha.2016.10.012, 2016.

Rousseau, D. D., Sima, A., Antoine, P., Hatté, C., Lang, A., and Zöller, L.: Link between European and North Atlantic abrupt climate changes over the last glaciation, Geophys. Res. Lett., 34, L22713, https://doi.org/10.1029/2007GL031716, 2007.

Rousseau, D.-D., Derbyshire, E., Antoine, P., and Hatté, C.: European Loess Records, Reference Module in Earth Systems and Environmental Sciences, Elsevier, Amsterdam, https://doi.org/10.1016/b978-0-12-409548-9.11136-4, 2018.

Sauer, D. and Felix-Henningsen, P.: Saprolite, soils, and sediments in the Rhenish Massif as records of climate and landscape history, Quaternary Int., 156–157, 4–12, https://doi.org/10.1016/j.quaint.2006.05.001, 2006.

Schad, P., Van Huyssteen, M., Anjos, L., Gaistordo, C., Deckers, J., Dondeyne, S., Eberhardt, E., Gerasimova, M., Harms, B., Jones, A., Krasilnikov, P., Reinsch, T., Vargas, T., and Zhang, G.: World reference base for soil resources 2014 International soil classification system for naming soils and creating legends for soil maps, 3rd Ed., edited by: Peter Schad, Cornie van Huyssteen, Erika Michéli, FAO, Rome (Italy), ISBN 978-92-5-108369-7, 2015.

Schaetzl, R. J., Bettis, E. A., Crouvi, O., Fitzsimmons, K. E., Grimley, D. A., Hambach, U., Lehmkuhl, F., Marković, S. B., Mason, J. A., Owczarek, P., Roberts, H. M., Rousseau, D.-D., Stevens, T., Vandenberghe, J., Zárate, M., Veres, D., Yang, S., Zech, M., Conroy, J. L., Dave, A. K., Faust, D., Hao, Q., Obreht, I., Prud'homme, C., Smalley, I., Tripaldi, A., Zeeden, C., and Zech, R.: Approaches and challenges to the study of loess – Introduction to the LoessFest Special Issue, Quaternary Res., 89, 563–618, https://doi.org/10.1017/qua.2018.15, 2018.

Schaffernicht, E. J., Ludwig, P., and Shao, Y.: Linkage between dust cycle and loess of the Last Glacial Maximum in Europe, Atmos. Chem. Phys., 20, 4969–4986, https://doi.org/10.5194/acp-20-4969-2020, 2020.

Schatz, A.-K., Qi, Y., Siebel, W., Wu, J., and Zöller, L.: Tracking potential source areas of Central European loess: examples from Tokaj (HU), Nussloch (D) and Grub (AT), Open Geosci., 7, 678–7, https://doi.org/10.1515/geo-2015-0048, 2015.

Schirmer, W.: Eine Klimakurve des Oberpleistozäns aus dem rheinischen Löss, E&G Quaternary Sci. J., 50, 25–49, https://doi.org/10.3285/eg.50.1.02, 2000.

Schirmer, W.: Rhine loess at Schwalbenberg II — MIS 4 and 3, E&G Quaternary Sci. J., 61, 32–47, https://doi.org/10.3285/eg.61.1.03, 2011.

Schmidt, C., Zeeden, C., Krauß, L., Lehmkuhl, F., and Zöller, L.: A chronological and palaeoenvironmental re-evaluation of two loess-palaeosol records in the northern Harz foreland, Germany, based on innovative modelling tools, Boreas, 50, 746–763, https://doi.org/10.1111/bor.12510, 2021.

Schubert, S., Jung, S., Pfänder, J. A., Hauff, F., and Garbe-Schönberg, D.: Petrogenesis of Tertiary continental intra-plate lavas between Siebengebirge and Westerwald, Germany: Constraints from trace element systematics and Nd, Sr and Pb isotopes, J. Volcanol. Geotherm. Res., 305, 84–99, https://doi.org/10.1016/J.JVOLGEORES.2015.08.023, 2015.

Schulte, P. and Lehmkuhl, F.: The difference of two laser diffraction patterns as an indicator for post-depositional grain size reduction in loess-paleosol sequences, Palaeogeogr. Palaeoclim. Palaeoecol., 509, 126–136, https://doi.org/10.1016/j.palaeo.2017.02.022, 2018.

Schulte, P., Lehmkuhl, F., Steininger, F., Loibl, D., Lockot, G., Protze, J., Fischer, P., and Stauch, G.: Influence of HCl pretreatment and organo-mineral complexes on laser diffraction measurement of loess–paleosol-sequences, CATENA, 137, 392–405, https://doi.org/10.1016/j.catena.2015.10.015, 2016.

Seelos, K., Sirocko, F., and Dietrich, S.: A continuous high-resolution dust record for the reconstruction of wind systems in central Europe (Eifel, Western Germany) over the past 133 ka, Geophys. Res. Lett., 36, L2072, https://doi.org/10.1029/2009GL039716, 2009.

Sheldon, N. D. and Tabor, N. J.: Quantitative paleoenvironmental and paleoclimatic reconstruction using paleosols, Earth-Sci. Rev., 95, 1–52, https://doi.org/10.1016/j.earscirev.2009.03.004, 2009.

Siebel, W., Eroğlu, S., Shang, C. K., and Rohrmüller, J.: Zircon geochronology, elemental and Sr-Nd isotope geochemistry of two Variscan granitoids from the Odenwald-Spessart crystalline complex (mid-German crystalline rise), Mineral. Petrol., 105, 187–200, https://doi.org/10.1007/s00710-012-0200-3, 2012.

Sirocko, F., Knapp, H., Dreher, F., Förster, M. W., Albert, J., Brunck, H., Veres, D., Dietrich, S., Zech, M., Hambach, U., Röhner, M., Rudert, S., Schwibus, K., Adams, C., and Sigl, P.: The ELSA-Vegetation-Stack: Reconstruction of Landscape Evolution Zones (LEZ) from laminated Eifel maar sediments of the last 60,000 years, Global Planet. Change, 142, 108–135, https://doi.org/10.1016/j.gloplacha.2016.03.005, 2016.

Smalley, I., O'Hara-Dhand, K., Wint, J., Machalett, B., Jary, Z., and Jefferson, I.: Rivers and loess: The significance of long river transportation in the complex event-sequence approach to loess deposit formation, Quaternary Int., 198, 7–18, https://doi.org/10.1016/j.quaint.2008.06.009, 2009.

Tarling, D. H. and Hrouda, F.: The Magnetic Anisotropy of Rocks, Chapman & Hall, London, 1993.

Taylor, S. N. and Lagroix, F.: Magnetic anisotropy reveals the depositional and postdepositional history of a loess-paleosol sequence at Nussloch (Germany): AMS of the Nussloch Loess-Paleosol Sequence, J. Geophys. Res.-Solid Earth, 120, 2859–2876, https://doi.org/10.1002/2014JB011803, 2015.

Taylor, S. N., Lagroix, F., Rousseau, D. D., and Antoine, P.: Mineral magnetic characterization of the upper pleniglacial nussloch loess sequence (Germany): An insight into local environmental processes, Geophys. J. Int., 199, 1463–1480, https://doi.org/10.1093/gji/ggu331, 2014.

Toucanne, S., Soulet, G., Freslon, N., Jacinto, R. S., Dennielou, B., Zaragosi, S., Eynaud, F., Bourillet, J.-F., and Bayon, G.: Millennial-scale fluctuations of the European Ice Sheet at the end of the last glacial, and their potential impact on global climate, Quaternary Sci. Rev., 123, 113–133, 2015.

Tricca, A., Stille, P., Steinmann, M., Kiefel, B., Samuel, J., and Eikenberg, J.: Rare earth elements and Sr and Nd isotopic compositions of dissolved and suspended loads from small river systems in the Vosges mountains (France), the river Rhine and groundwater, Chem. Geol., 160, 139–158, https://doi.org/10.1016/S0009-2541(99)00065-0, 1999.

Újvári, G., Varga, A., Ramos, F. C., Kovács, J., Németh, T., and Stevens, T.: Evaluating the use of clay mineralogy, Sr–Nd isotopes and zircon U–Pb ages in tracking dust provenance: An example from loess of the Carpathian Basin, Chem. Geol., 304–305, 83–96, https://doi.org/10.1016/j.chemgeo.2012.02.007, 2012.

Újvári, G., Kok, J. F., Varga, G., and Kovács, J.: The physics of wind-blown loess: Implications for grain size proxy interpretations in Quaternary paleoclimate studies, Earth-Sci. Rev., 154, 247–278, https://doi.org/10.1016/j.earscirev.2016.01.006, 2016.

Újvári, G., Stevens, T., Molnár, M., Demény, A., Lambert, F., Varga, G., Jull, A. J. T., Páll-Gergely, B., Buylaert, J.-P., and Kovács, J.: Coupled European and Greenland last glacial dust activity driven by North Atlantic climate, P. Natl. Acad. Sci. USA, 114, E10632–E10638, https://doi.org/10.1073/pnas.1712651114, 2017.

Újvári, G., Klötzli, U., Stevens, T., Svensson, A., Ludwig, P., Vennemann, T., Gier, S., Horschinegg, M., Palcsu, L., Hippler, D., Kovács, J., Di Biagio, C., and Formenti, P.: Greenland Ice Core Record of Last Glacial Dust Sources and Atmospheric Circulation, J. Geophys. Res.-Atmos., 127, e2022JD036597, https://doi.org/10.1029/2022JD036597, 2022.

Vandenberghe, J.: Grain size of fine-grained windblown sediment: A powerful proxy for process identification, Earth-Sci. Rev., 121, 18–30, https://doi.org/10.1016/j.earscirev.2013.03.001, 2013.

Vandenberghe, J., Mücher, H., Roebroeks, W., and Gemke, D.: Lithostratigraphy and palaeoenvironment of the Pleistocene deposits at Maastricht-Belvédère, southern Limburg, the Netherlands, Analecta Praehistorica Leidensia 18-Maastricht-Belvédère: Stratigraphy, palaeoenvironment and archaeology of the middle and late pleistocene deposits, Analecta Praehist. Leiden, 18, 7–18, 1985.

Vandenberghe, J., Zhisheng, A., Nugteren, G., Huayu, L., and Van Huissteden, K.: New absolute time scale for the Quaternary climate in the Chinese Loess region by grain-size analysis, Geology, 25, 35–38, https://doi.org/10.1130/0091-7613(1997)025<0035:NATSFT>2.3.CO;2, 1997.

Vinnepand, M., Fischer, P., Fitzsimmons, K., Thornton, B., Fiedler, S., and Vött, A.: Combining Inorganic and Organic Carbon Stable Isotope Signatures in the Schwalbenberg Loess-Palaeosol-Sequence Near Remagen (Middle Rhine Valley, Germany), Front. Earth Sci., 8, 276, https://doi.org/10.3389/feart.2020.00276, 2020.

Vinnepand, M., Fischer, P., Jöris, O., Hambach, U., Zeeden, C., Schulte, P., Fitzsimmons, K. E., Prud'homme, C., Perić, Z., Schirmer, W., Lehmkuhl, F., Fiedler, S., and Vött, A., Decoding geochemical signals of the Schwalbenberg Loess-Palaeosol-Sequences – A key to Upper Pleistocene ecosystem responses to climate changes in western Central Europe, Catena, 212, 106076, https://doi.org/10.1016/j.catena.2022.106076, 2022.

von Suchodoletz, H., Kühn, P., Hambach, U., Dietze, M., Zöller, L., and Faust, D.: Loess-like and palaeosol sediments from Lanzarote (Canary Islands/Spain) – Indica-

tors of palaeoenvironmental change during the Late Quaternary, Palaeogeogr. Palaeoclimatol. Palaeoecol., 278, 71–87, https://doi.org/10.1016/j.palaeo.2009.03.019, 2009.

Wang, Y.-X., Yang, J.-D., Chen, J., Zhang, K.-J., and Rao, W.-B.: The Sr and Nd isotopic variations of the Chinese Loess Plateau during the past 7 Ma: Implications for the East Asian winter monsoon and source areas of loess, Palaeogeogr. Palaeoclimatol. Palaeoecol., 249, 351–361, https://doi.org/10.1016/j.palaeo.2007.02.010, 2007.

Weltje, G. J., Bloemsma, M. R., Tjallingii, R., Heslop, D., Röhl, U., and Croudace, I. W.: Prediction of Geochemical Composition from XRF Core Scanner Data: A New Multivariate Approach Including Automatic Selection of Calibration Samples and Quantification of Uncertainties, in: Micro-XRF Studies of Sediment Cores: Applications of a non-destructive tool for the environmental sciences, edited by: Croudace, I. W. and Rothwell, R. G., Springer Netherlands, Dordrecht, 507–534, https://doi.org/10.1007/978-94-017-9849-5_21, 2015.

Wörner, G., Staudigel, H., and Zindler, A.: Isotopic constraints on open system evolution of the Laacher See magma chamber (Eifel, West Germany), Earth Planet. Sci. Lett., 75, 37–49, https://doi.org/10.1016/0012-821X(85)90048-2, 1985.

Zech, M., Zech, R., Zech, W., Glaser, B., Brodowski, S., and Amelung, W.: Characterisation and palaeoclimate of a loess-like permafrost palaeosol sequence in NE Siberia, Geoderma, 143, 281–295, https://doi.org/10.1016/j.geoderma.2007.11.012, 2008.

Zeeden, C. and Hambach, U.: Magnetic Susceptibility Properties of Loess From the Willendorf Archaeological Site: Implications for the Syn/Post-Depositional Interpretation of Magnetic Fabric, Front. Earth Sci., 8, 599491, https://doi.org/10.3389/feart.2020.599491, 2021.

Zeeden, C., Hambach, U., and Händel, M.: Loess magnetic fabric of the Krems-Wachtberg archaeological site, Quaternary Int., 372, 188–194, https://doi.org/10.1016/j.quaint.2014.11.001, 2015.

Zeeden, C., Hambach, U., Obreht, I., Hao, Q., Abels, H. A., Veres, D., Lehmkuhl, F., Gavrilov, M. B., and Marković, S. B.: Patterns and timing of loess-paleosol transitions in Eurasia: Constraints for paleoclimate studies, Global Planet. Change, 162, 1-7, https://doi.org/10.1016/j.gloplacha.2017.12.021, 2018.

Zens, J., Zeeden, C., Römer, W., Fuchs, M., Klasen, N., and Lehmkuhl, F.: The Eltville Tephra (Western Europe) age revised: Integrating stratigraphic and dating information from different Last Glacial loess localities, Palaeogeogr. Palaeoclimatol. Palaeoecol., 466, 240–251, https://doi.org/10.1016/j.palaeo.2016.11.033, 2017.

Zhang, Q., Appel, E., Stanjek, H., Byrne, J. M., Berthold, C., Sorwat, J., Rösler, W., and Seemann, T.: Humidity related magnetite alteration in an experimental setup, Geophys. J. Int., 224, 69–85, https://doi.org/10.1093/gji/ggaa394, 2021.

Zhang, R., Kravchinsky, V. A., Zhu, R., and Yue, L.: Paleomonsoon route reconstruction along a W–E transect in the Chinese Loess Plateau using the anisotropy of magnetic susceptibility: Summer monsoon model, Earth Planet. Sci. Lett., 299, 436–446, https://doi.org/10.1016/j.epsl.2010.09.026, 2010.

Zhu, X., Liu, L., Wang, X., and Ji, J.: The Sr-Nd isotope geochemical tracing of Xiashu Loess and its implications for the material transport mechanism of the Yangtze River, CATENA, 203, 105335, https://doi.org/10.1016/j.catena.2021.105335, 2021.